Marine Chemistry 235 (2021) 104008

Contents lists available at ScienceDirect

Marine Chemistry

journal homepage: www.elsevier.com/locate/marchem

Tracing Circumpolar Deep Water and glacial meltwater using humic-like fluorescent dissolved organic matter in the Amundsen Sea, Antarctica

Mi Hae Jeon [a,b], Jinyoung Jung [a,*], Mi Ok Park [b,*], Shigeru Aoki [c], Tae-Wan Kim [a], Seung-Kyu Kim [d]

[a] Division of Polar Ocean Sciences, Korea Polar Research Institute, 26, Songdomirae-ro, Yeonsu-gu, Incheon 21990, Republic of Korea
[b] Department of Oceanography, Pukyong National University, Yongso-ro, Nam-gu, Busan 48513, Republic of Korea
[c] Institute of Low Temperature Science, Hokkaido University, Sapporo 060-0819, Japan
[d] Department of Marine Science, Incheon National University, 119, Academy-ro, Yeonsu-gu, Incheon 22012, Republic of Korea

ARTICLE INFO

Keywords:
Amundsen Sea
Fluorescent dissolved organic matter
Humic-like component
CDW
Glacial meltwater

ABSTRACT

The Amundsen Sea is the most rapidly melting part of the West Antarctic Ice Sheet, due to increased heat transport by Circumpolar Deep Water (CDW). Tracing CDW and resulting glacial meltwater is important since glacial meltwater may change the water mass properties, leading to the change of the biogeochemical cycles. In this study, in order to investigate the potential for using the humic-like component of fluorescent dissolved organic matter (FDOM) as a tracer for CDW and glacial meltwater in the Amundsen Sea, a hydrographic survey was conducted during the austral summer of 2018 aboard the Korean icebreaker IBR/V *Araon*. The meteoric water and CDW fractions calculated using the humic-like component (f_{mw_humic} and f_{cdw_humic}) were compared to those using oxygen isotope ($\delta^{18}O$) (f_{mw}) and optimum multiparameter analysis (OMP) (f_{cdw_OMP}), respectively. The fluorescence intensity of the humic-like component varied from 0.007 to 0.021, with higher values in the deeper layer and lower intensities in the surface waters. The range of f_{cdw_humic} (0.5–1.0) was narrower than that of f_{cdw_OMP} (0.1–1.0), indicating that the f_{cdw_humic} values were overestimated due to the remained humic-like C1. To minimize the effect of the remained humic-like C1 on the calculation of CDW fraction, we used newly derived empirical equations (i.e., $f_{cdw\_OMP} = 105.17 \times C1–1.14$ for transect 1 and $f_{cdw\_OMP} = 126.04 \times C1–1.41$ for transect 2). The CDW fraction calculated using the empirical equations ($f_{cdw\_humic\_empirical}$) was in good agreement with the f_{cdw_OMP}. We also found a significant positive relationship between f_{mw} and f_{mw_humic}, indicating that a reasonable method can be applied with a high percentage of explained variance and that f_{mw} can be largely explained by f_{mw_humic}. Our results show that the humic-like component can be a useful tracer for identifying CDW and glacial meltwater in the Amundsen Sea.

1. Introduction

The ice sheet around West Antarctica has undergone widespread losses in recent decades (Rignot et al., 2008; Pritchard et al., 2012) that increased from 53 ± 29 Gt/yr during the 1990s to 159 ± 26 Gt/yr during the 2010s (Shepherd et al., 2018). The Amundsen Sea, located in West Antarctica, is the most rapidly melting part of the West Antarctic Ice Sheet (Rignot et al., 2008; Pritchard et al., 2012). The main driver of melting in the Amundsen Sea is thought to be Circumpolar Deep Water (CDW) that originates from the Antarctic Circumpolar Current (ACC). The intrusion of warm, salty CDW into the Amundsen Sea through the Dotson Trough induces melting through latent heat transfer to the floating ice shelves, resulting in accelerated glacial melting in this region (Jenkins et al., 2010; Jacobs et al., 2011). As the CDW reaches the glacier and ice shelves, the warm CDW melts the ice and forms a modified CDW (mCDW) (Jenkins et al., 2010; Jacobs et al., 2012; Miles et al., 2016). The resulting mCDW dilution by glacial meltwater initiates a circulation pattern whereby fresher and cooler mCDW flows up the underside of the floating ice sheets and returns to the open sea higher in the water column (Alderkamp et al., 2015).

The Amundsen Sea Polynya (ASP) is the most productive polynya among the 37 identified coastal polynya systems in the Antarctic (Arrigo and van Dijken, 2003) due to the supply of iron provided by the melting sea ice and/or glaciers (Gerringa et al., 2012; Alderkamp et al., 2015). In

* Corresponding authors.
E-mail addresses: jinyoungjung@kopri.re.kr (J. Jung), mopark@pknu.ac.kr (M.O. Park).

https://doi.org/10.1016/j.marchem.2021.104008
Received 8 July 2020; Received in revised form 22 June 2021; Accepted 23 June 2021
Available online 12 July 2021

addition, glacial meltwater can affect ocean circulation and stratification because it is less dense than the underlying water (Jourdain et al., 2017; Silvano et al., 2018). Thus, an increase in glacial meltwater input to the ASP has the potential to alter the biogeochemical and physical properties of the Amundsen Sea. Therefore, it is crucial to trace this glacial meltwater produced by the inflow of CDW.

Considerable effort has been devoted to tracing glacial meltwater in the Amundsen Sea using chemical tracers such as stable oxygen isotopic ratios ($\delta^{18}O$) (Randall-Goodwin et al., 2015) and noble gases (e.g., helium and neon) (Kim et al., 2016; Biddle et al., 2019). Randall-Goodwin et al. (2015) demonstrated that the fraction of meteoric water, including precipitation and glacial meltwater, exhibited maximum values of 2–3% and that the glacial meltwater fraction, determined separately from the meteoric water, had maximum values of 1–2%, with the highest value (2.1%) located at the Dotson Ice Shelf outflow. Kim et al. (2016) reported that the calculated glacial meltwater fraction in the Amundsen Sea using noble gases ranged from 0.3–2.0%, which is similar to the findings of Randall-Goodwin et al. (2015). However, analyses of $\delta^{18}O$ and noble gases are expensive and labor intensive. Additionally, estimating the meltwater fraction using noble gases has limitations related to gas loss in the upper layer (< 200 m) via air–sea gas exchange (Kim et al., 2016).

Fluorescent dissolved organic matter (FDOM), which is a fraction of dissolved organic matter (DOM), absorbs and re-emits light as fluorescence (Mopper et al., 1996; Stedmon and Nelson, 2015). Excitation and emission fluorescence spectra can provide useful information regarding the origin and composition of the DOM. Typically, FDOM is characterized by two major types: amino acid-like compounds and humic-like compounds (Coble, 2007). Because the humic-like compounds are resistant to biological degradation (Thurman, 1985; Ishii and Boyer, 2012; Mendoza et al., 2017) and vulnerable to photochemical degradation by sunlight (Chen and Bada, 1992; Yamashita et al., 2010; Chari et al., 2013; Logvinova et al., 2015; Kida et al., 2019), it has a long residence time (centuries to millennia) in the water column, except for in the surface layer (Yamashita and Tanoue, 2008). In addition, previous studies have reported that the humic-like component exhibit conservative mixing behavior in estuarine (Zhu et al., 2018), coastal (Yamashita et al., 2008, 2011; Zhu et al., 2018), and oceanic systems (Osburn and Stedmon, 2011; Tanaka et al., 2016; Kim et al., 2019; Jung et al., 2021). These results indicate that the conservative behavior of the humic-like component of FDOM can be used as a tracer to identify water masses (Gonçalves-Araujo et al., 2016). Furthermore, unlike analyses of $\delta^{18}O$ and noble gases in seawater samples, a key advantage of FDOM analysis is that it can be analyzed with a high-sensitivity, despite small sample quantities.

Recently, Kim et al. (2019) reported that FDOM is a reliable tracer for identifying water masses in the deep Indian Ocean. Furthermore, Gonçalves-Araujo et al. (2016) used FDOM to trace freshwater in Arctic surface waters. Although these previous studies provide evidence that FDOM can be a useful tracer for identifying water masses or freshwater discharge, little is known about the ability of the humic-like component to act as a tracer for CDW and glacial meltwater in the Antarctic Ocean. In this study, we report on the distributions of FDOM, sea ice melt, and glacial meltwater calculated using $\delta^{18}O$, coupled with hydrographic properties in the Amundsen Sea. The objective of this study is to examine the possibility of using FDOM as a tracer of CDW and glacial meltwater in the Amundsen Sea.

2. Materials and methods

2.1. Hydrographic survey

A hydrographic survey was conducted in the Amundsen Sea during the ANA08B cruise (January 18– February 2, 2018) aboard the Korean icebreaker IBR/V *Araon* (Fig. 1). The cruise track covered the oceanic area (OA), the marginal sea ice zone (MSIZ), the ASP, the Dotson ice shelf (DIS), and the Getz ice shelf (GIS). In order to survey the spatial distributions of CDW and glacial meltwater, the sampling stations were divided into two transects: transect 1 across the oceanic area (OA), the marginal sea ice zone (MSIZ), the Amundsen Sea polynya (ASP), and the Dotson ice shelf (DIS), which is a known pathway of CDW intrusion (Ha et al., 2014); and transect 2 in front of the western Getz ice shelf (GIS).

Seawater sampling was conducted at 19 stations using twenty-four 10 L Niskin bottles attached to a rosette sampler. Vertical profiles of salinity, temperature, and dissolved oxygen were obtained from the conductivity-temperature-depth (CTD) sensors (SeaBird Electronics, SBE 911 plus, USA). During the cruise, the oxygen sensor data were independently calibrated against discrete samples collected for dissolved oxygen titrations using the Winkler titration method (Carpenter, 1965). The mixed layer depth (MLD) was defined as the shallowest

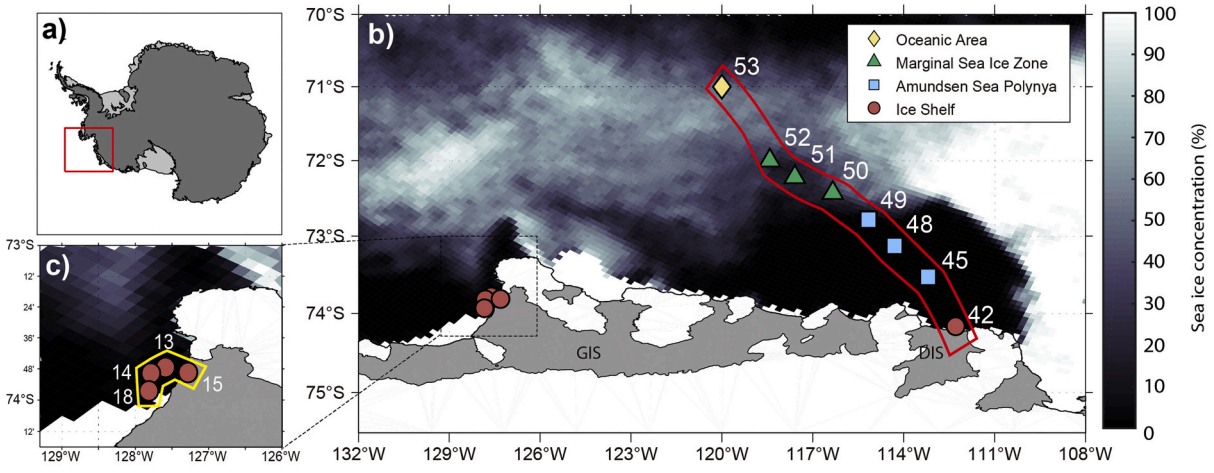

Fig. 1. (a) The location of the study area in Antarctica. (b) hydrographic survey locations in the Amundsen Sea. The locations of the sampling stations are superimposed onto the mean sea ice concentrations derived from Advanced Microwave Scanning Radiometer for EOS (AMSR-E) using the ARTIST Sea Ice (ASI) algorithm from January 18 to February 2, 2018 in the Amundsen Sea during the ANA08B cruise. Geographic locations are divided into the oceanic area (OA, yellow diamond), marginal sea ice zone (MSIZ, green triangles), Amundsen Sea polynya (ASP, blue squares), and ice shelf (red circles) based on the mean sea ice concentrations and distributions. Transect 1 cuts across the OA, MSIZ, ASP, and Dotson ice shelf (DIS), and transect 2 is in front of the western Getz ice shelf (GIS), which are enclosed by the red and yellow lines, respectively. (c) enlarged view of the sampling stations in front of the GIS. (For interpretation of the references to colour in this figure legend, the reader is referred to the web version of this article.)

depth at which the density exceeded 0.02 kg m^{-3} relative to surface density (Cisewski et al., 2008; Alderkamp et al., 2012). The euphotic zone depth (EZD) was estimated as the depth at which 1% of the surface photosynthetic available radiation (PAR) remains (Kirk, 1994).

Seawater samples for inorganic nutrients were drawn from the Niskin bottles into 50 mL conical tubes and immediately stored in a refrigerator at 4 °C prior to chemical analysis. Seawater samples for particulate organic carbon (POC) measurements were collected directly from the Niskin bottle into a pre-rinsed amber polyethylene bottle. Known volumes (500 mL to 1 L) of seawater were filtered onto pre-combusted (at 550 °C for 6 h) Whatman GF/F filters (47 mm diameter) using a filtering system under a gentle vacuum at <0.1 MPa. The GF/F filters were stored at −80 °C until the analyses were conducted in the onshore laboratory. Seawater samples for dissolved organic carbon (DOC), FDOM, and $\delta^{18}O$ analyses were drawn from the Niskin bottles using gravity filtration through inline pre-combusted (at 550 °C for 6 h) Whatman GF/F filters (47 mm diameter) and kept in acid-washed (0.1 M HCl) polycarbonate 47 mm filter holders (PP-47, ADVANTEC). The filter holders were connected directly to the Niskin bottle spigots. The filtrates were collected in acid-washed glass bottles and divided into pre-combusted (at 550 °C for 6 h) 20 ml glass ampoules and pre-washed glass vials using a sterilized serological pipette. The glass ampoules for DOC and FDOM measurements were sealed with a torch, flash-frozen, and stored at −24 °C until the onshore analyses were conducted. For the $\delta^{18}O$ samples, the glass vials were sealed with parafilm in order to prevent the entry of air and stored at 4 °C until the onshore analyses were conducted.

It is worth noting that the ideal method for measurement of FDOM is to analyze without freezing. However, given the remoteness of sampling area, delays between sampling and analysis of more than 2 months were inevitable. Previous studies investigated the impact of freezing on FDOM in aquatic environments (Castillo and Coble, 2000; Spencer et al., 2007; Fellman et al., 2008; Rochelle-Newall et al., 2014); however, the results of these studies are somewhat contradictory: Some indicated that the freezing/thawing optical samples result in fading of fluorescence in freshwater environments, because dissolved organic matter could not be redissolved during freezing/thawing process (Spencer et al., 2007; Fellman et al., 2008). On the other hand, others demonstrated no statistically significant difference between fresh (non-frozen) and frozen samples in coastal and marine environments (Castillo and Coble, 2000; Rochelle-Newall et al., 2014). Rochelle-Newall et al. (2014), who compared samples prior to freezing with samples frozen for 6 months, reported that there is some scatter along the 1:1 line (intercept = 0.38, slope = 0.997, $r^2 = 0.91$, $p < 0.001$). Furthermore, loss of fluorescence from freezing especially occurs when samples contain a high CDOM concentration (Coble and Nelson, 2009). However, the absorbance values of all samples in this study were below 0.3 cm^{-1} at 254 nm. Therefore, the loss of fluorescence from freezing is likely negligible.

2.2. Measurements

2.2.1. Inorganic nutrients

Inorganic nutrients, including nitrite + nitrate ($NO_2 + NO_3$), phosphate (PO_4), ammonium (NH_4), and silicic acid ($Si(OH)_4$), were measured during the cruise using a four-channel Auto-Analyzer (QuAAtro, Seal Analytical, Germany), according to the Joint Global Ocean Flux Study (JGOFS) protocols described by Gordon et al. (1993). The precisions for the $NO_2 + NO_3$, PO_4, NH_4, and $Si(OH)_4$ measurements were ± 0.14, ± 0.02, ± 0.18, and ± 0.28 μmol kg^{-1}, respectively.

2.2.2. Particulate organic carbon

Before POC analyses, the filter samples were freeze-dried, then exposed to hydrochloric acid (HCl) fumes for 24 h in a desiccator to remove inorganic carbon from the samples. Measurements were conducted with a CHN elemental analyzer (vario Macro cube, Elementar, Germany). Acetanilide was used as a standard. The precision of these measurements was ±4% (Jung et al., 2020).

2.2.3. Fluorescent dissolved organic matter

Fluorescence excitation-emission matrices (EEMs) of each sample were obtained using a fluorescence spectrophotometer (F-7000, Hitachi) with a 1 cm quartz cuvette. The excitation (Ex) spectra were scanned from 250 to 500 nm at 5 nm intervals, while the emission (Em) spectra were scanned from 280 to 550 nm at 1 nm intervals. The fluorescence intensity of Milli-Q water was measured daily and used as a blank for quality control. The EEMs of each sample were calibrated by subtracting the EEM of the Milli-Q water and were normalized to Raman Units (R.U.) by integrating the Raman bands from 380 to 420 nm at a 350 nm excitation (Stedmon et al., 2003). If the absorbance value of a sample is higher than 0.3 cm^{-1} at 254 nm, the sample needs to be diluted with Milli-Q water (Burdige et al., 2004) to remove an inner filter effect. In this study, the inner filter effect was neglected because the absorbance values of all samples measured using a spectrophotometer (Lambda 365, PerkinElmer) were below 0.3 cm^{-1}. The obtained EEMs were modeled using parallel factor analysis (PARAFAC) in MATLAB (Mathworks, USA) with the DOMFluor toolbox (Stedmon and Bro, 2008). The number of components was determined based on the split-half validation (Chen et al., 2019). The best PARAFAC model was obtained with three components, having 96.2% of explained variance.

2.2.4. Dissolved organic carbon

DOC analysis was conducted with high-temperature combustion using a TOC analyzer (TOC-L, Shimadzu). On a daily basis, Milli-Q water blanks and consensus reference material (CRM, 42–45 μM C, deep Florida Strait water obtained from the University of Miami) were measured every sixth analysis for quality assurance and quality control (QA/QC). Based on repeated measurements (at least three measurements per sample), analytical errors were within 5% for DOC (Chen et al., 2018; Jung et al., 2021).

2.2.5. Stable oxygen isotope ratios

Samples for $\delta^{18}O$ analysis were shaken automatically for ~8 h in an 18 °C water bath to equilibrate with CO_2 (Nakayama et al., 2014). $\delta^{18}O$ analyses were conducted using a mass spectrometer (Finnigan DELTA plus, Germany) coupled with an equilibrium device at the Institute of Low Temperature Science, Hokkaido University, Japan. $\delta^{18}O$ was determined with respect to the Vienna-Standard Mean Ocean Water (V-SMOW) standard. The $\delta^{18}O$ was obtained as follows:

$$\delta^{18}O = \left[\left({}^{18}O/{}^{16}O_{sample}/{}^{18}O/{}^{16}O_{V-SMOW}\right)-1\right] \times 1000 \quad (1)$$

The accuracy of the analysis was estimated to be 0.02‰ based on duplicate measurements (Nakamura et al., 2014).

2.2.6. Stable oxygen isotope for quantifying freshwater sources

$\delta^{18}O$ and salinity were used to determine the fractions of sea ice meltwater, meteoric water, and seawater, following the approach developed by (Östlund and Hut, 1984). Assuming that the water in the study area is a mixture of sea ice meltwater (f_{sim}), meteoric water (f_{mw}), and seawater (f_{sw}), the fractions of each of these water masses were calculated using the following mass balance equations:

$$\begin{aligned} f_{sim} + f_{mw} + f_{sw} &= 1 \\ f_{sim}\cdot S_{sim} + f_{mw}\cdot S_{mw} + f_{sw}\cdot S_{sw} &= S_{obs} \\ f_{sim}\cdot \delta^{18}O_{sim} + f_{mw}\cdot \delta^{18}O_{mw} + f_{sw}\cdot \delta^{18}O_{sw} &= \delta^{18}O_{obs} \end{aligned} \quad (2)$$

where f and S refer to the fraction and salinity, respectively. $\delta^{18}O_{obs}$ and S_{obs} are the observed values from each seawater sample. Sea ice formation, which injects brine into the underlying seawater, will be represented by a negative f_{sim} (Meredith et al., 2008). The $\delta^{18}O$ and S values for the three end-member water masses used in the calculations are summarized in Table 1. For further details on the selection of the three end-members applicable to the Amundsen Sea region, refer to Randall-

Table. 1
End-member properties used for the water masses in the Amundsen Sea.

	Salinity	$\delta^{18}O$ (‰)	Reference
[a]Circumpolar Deep Water (CDW)	34.73	−0.070	This study
Meteoric Water (MW)	0	−25	Randall-Goodwin et al. (2015)
Sea Ice Meltwater (SIM)	7	2.1	

[a] We used a salinity of 34.73 and a δ18O of −0.070‰ as the end-members for CDW, which were measured in the deep layer in the oceanic area (OA) where pure CDW is located.

Goodwin et al. (2015).

2.2.7. Optimum multiparameter analysis for quantifying water mass fraction

As shown in Eq. (2), the $\delta^{18}O$ method is based on the assumption that water masses in the Amundsen Sea are composed of sea ice meltwater, meteoric water, and seawater, including AASW, WW, and CDW. To quantify the CDW fraction, the end-members of $\delta^{18}O$ and S values for each water mass are necessary. However, due to the lack of the $\delta^{18}O$ end-members for AASW and WW, we could not calculate the CDW fraction by using Eq. (2). Therefore, additional analysis is required, and we chose the optimum multiparameter (OMP) analysis previously applied to identifying the distribution and mixing of water masses in diverse regions of the ocean (Tomczak and Large, 1989; Poole and Tomczak, 1999; Budillon et al., 2003, 2010; Pardo et al., 2012; Frants et al., 2013; Biddle et al., 2017).

OMP analysis starts with the definitions of water masses and water types. As described in detail in Tomczak and Large (1989), water mass is physical entity of finite volume, and water type is defined as points in parameter space. Briefly, OMP analysis is based on the assumption that all water masses are a mixture of the water types. The fractions of water types were derived using the following equation:

$$G \cdot x - d = r$$
$$\begin{pmatrix} S_{mw} & S_{ww} & S_{cdw} \\ \theta_{mw} & \theta_{ww} & \theta_{cdw} \\ DO_{mw} & DO_{ww} & DO_{cdw} \\ 1 & 1 & 1 \end{pmatrix} \cdot \begin{pmatrix} f_{mw} \\ f_{ww} \\ f_{cdw} \end{pmatrix} - \begin{pmatrix} S_{obs} \\ \theta_{obs} \\ DO_{obs} \\ 1 \end{pmatrix} = \begin{pmatrix} r_S \\ r_\theta \\ r_{DO} \\ r_{mass} \end{pmatrix} \quad (3)$$

where G is a matrix with the parameter values for the source water types (SWT), x is a vector of relative contributions for water types, d is a vector of the observed values, and r is the residual value. OMP analysis has two following assumptions: (a) the water masses are a mixture of the water types, and (b) the sum of all contributions should be 100%. The fractions of the water types were calculated using the least squares method for minimizing the residual. A nonnegativity constraint is also applied, as fractions of water types must have positive values.

OMP analysis requires the parameter values (typically potential temperature (θ), S, and dissolved oxygen (DO) concentration) of each SWT. In this study, we used values reported by Biddle et al. (2017). AASW is excluded from the OMP analysis due to the difficulty of end-member selection, so OMP analysis is only applied below 75 m (Biddle et al., 2017).

3. Results and discussion

3.1. Fluorescent dissolved organic matter components

Three components were identified by the PARAFAC model (Fig. 2) and compared with those in the OpenFluor database (Table. S1) (Murphy et al., 2013). Component 1 (C1) has an excitation maximum below 250 nm with a broad emission spectrum, similar to a terrestrial humic-like fluorophore (Coble, 1996; Stedmon et al., 2003; Dubnick et al., 2010; Osburn and Stedmon, 2011). Component 2 (C2, Ex/Em = 275/340 nm) is similar to a tryptophan-like fluorophore (Coble, 1996; Dubnick et al., 2010; Stedmon et al., 2011; Chen et al., 2018). Component 3 (C3, Ex/Em ≤ 250(300)/359 nm) spectra represent sea ice related protein-like fluorophores (Chen et al., 2018). Because DOC is known as a

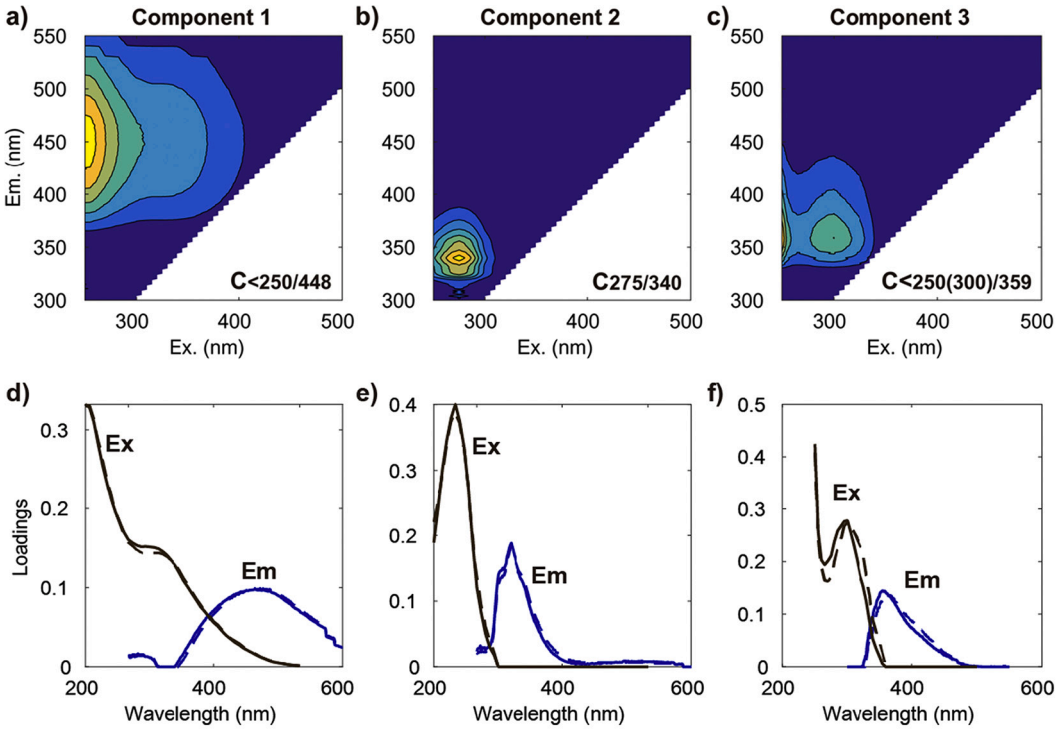

Fig. 2. EEM contour plots of (a–c) the three different fluorescent components C1–C3 identified by PARAFAC in the seawater samples collected from the Amundsen Sea, with the excitation (brown lines) and emission (blue lines) spectra of three components (d–f). The solid and dashed lines denote two random halves of the complete dataset. (For interpretation of the references to colour in this figure legend, the reader is referred to the web version of this article.)

reliable proxy for DOM (Thurman, 1985; Jiang et al., 2018), DOC concentrations were compared with C1 fluorescence intensities to evaluate the data quality and contamination of FDOM (Fig. S1). DOC concentrations ranged from 36 to 49 μM C (mean: 42 ± 2 μM C) in the upper 100 m and 37 to 45 μM C (mean: 40 ± 2 μM C) in the deeper layer (i.e., below ~100 m). Despite the massive phytoplankton blooms in the Amundsen Sea during the austral summer (Arrigo and van Dijken, 2003; Park et al., 2017), the DOC concentrations in the upper 100 m were somewhat lower than those (46 ± 3 and 55 ± 5 μM C) observed in the Ross Sea (Carlson et al., 2000), suggesting a low surface accumulation of DOC in the Amundsen Sea due to the nonlimiting macronutrients in the Antarctic waters and bio-labile and photo-labile nature of freshly produced DOC (Chen et al., 2019). The DOC concentrations in the deeper layer were comparable to the results by Fang et al. (2020), who reported that the DOC concentrations in the deeper layer (i.e., below ~100 m) of the Amundsen Sea ranged between 39 and 50 μM C, with an average of 43 ± 3 μM C, suggesting that the DOC cycling in the Amundsen Sea is dynamic (Fang et al., 2020). However, the deep DOC concentrations near the seafloor (i.e., below ~400 m) observed in both this study (40 ± 1.9 μM C) and Fang et al. (2020) (42 ± 2 μM C) were similar to those (41.8 ± 0.8 μM C) observed in the Ross Sea (Carlson et al., 2000). A detailed description of the rapid cycling of DOC in the Amundsen Sea is provided by Fang et al. (2020). Briefly, deep DOC supplied to the surface layer via CDW intrusion and mixing with the overlying water is consumed by microbial and/or photochemical degradation along with fresh DOC produced by primary production (Shen and Benner, 2018). The DOC is redistributed vertically by water mixing due to brine rejection during sea ice formation in winter, implying that the DOC reservoir has a relatively short turnover time on the order of years (Fang et al., 2020). The results mentioned above suggest that our results for DOC concentration reflect the characteristics of DOC in the Amundsen Sea. In addition, C1 fluorescence intensities in the surface were generally lower than the values in the deeper layers, which is consistent with previous studies (Chen and Bada, 1992; Determann et al., 1996; Stedmon and Markager, 2005a; Yamashita et al., 2007). These results indicated that no FDOM contamination had occurred. Although the three components were identified in the seawater samples; in this study, we used only C1 to demonstrate the potential for the humic-like component of FDOM to act as a tracer of CDW and glacial meltwater in the Amundsen Sea.

3.2. *Spatial distributions of freshwater fractions and the humic-like component*

The spatial distributions of sea surface temperature (SST) and salinity (SSS), water fractions (f_{mw} and f_{sim}), and the humic-like component C1 in the surface layer are shown in Fig. 3. The SST and SSS ranged from −1.6 to −0.6 °C and 33.0 to 34.0, respectively (Fig. 3a and b). The highest SSS values were observed in front of the ice shelves, but the SSTs exhibited slightly lower values (~ −1.0 °C) compared to other regions (i.e., OA, MSIZ, and ASP). Alderkamp et al. (2015) reported that the meltwater-laden mCDW has a SSS of <34.0 and a SST between −1.1 and − 0.5 °C near the coast of the Amundsen Sea, which are similar to the SSS and SST values observed in front of the ice shelves in this study, suggesting the upwelling of meltwater-laden mCDW (Miles et al., 2016). The SST and SSS gradually decreased from the DIS toward the OA along transect 1 due to the influences of meteoric water and sea ice meltwater.

The f_{mw} varied from 0.020 to 0.027, with higher values observed in the ASP and DIS (Fig. 3c), indicating that CDW-generated glacial meltwater is delivered from the DIS to the ASP region by a geostrophically-driven outflow (Jenkins et al., 2010; Jacobs et al., 2011). In addition, the values of f_{mw} in the DIS were higher than those in the western GIS. The differences in f_{mw} values among the ice shelf regions presumably reflect regional differences in the magnitude and duration of sub-glacial

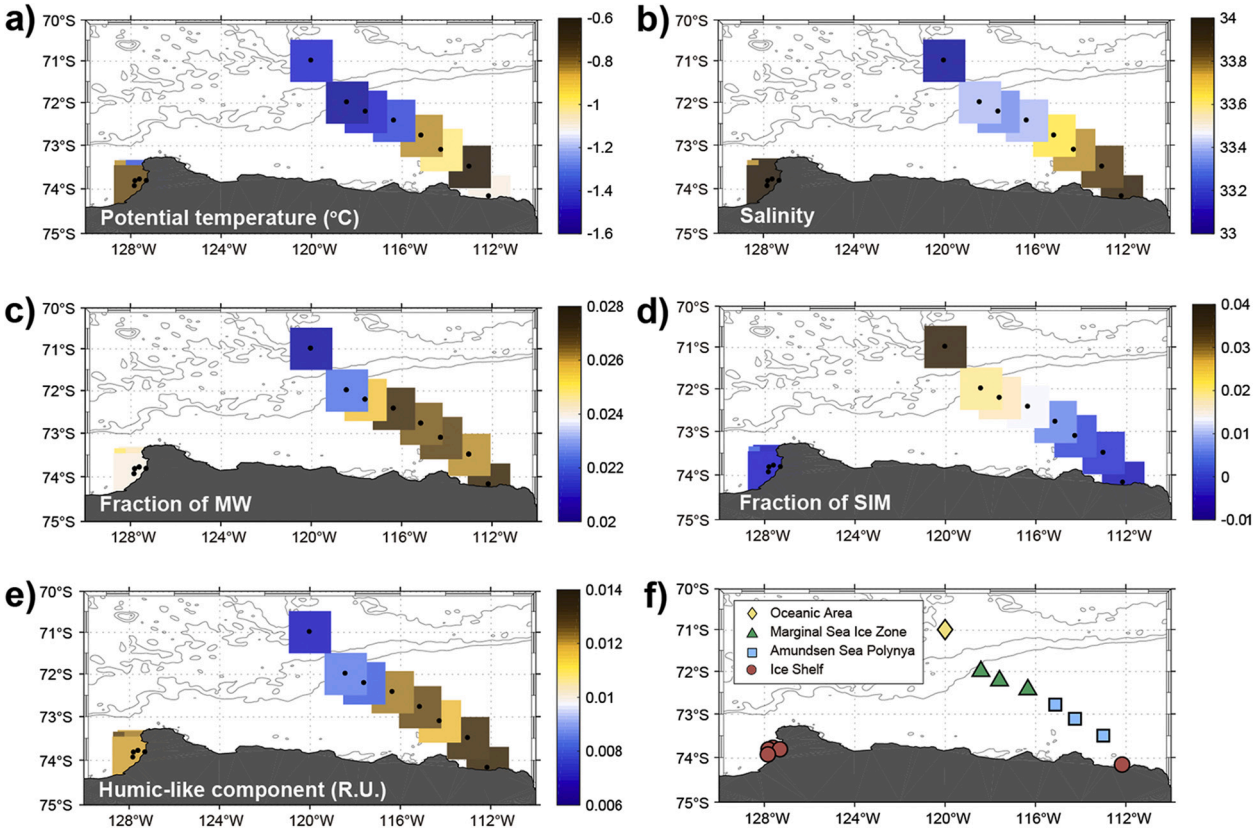

Fig. 3. Spatial distributions of sea surface (a) temperature (°C), (b) salinity, (c) meteoric water (f_{mw}), (d) sea ice meltwater (f_{sim}) fractions, (e) the humic-like component (R.U.), and (f) geographic sampling locations in the Amundsen Sea.

melting due to CDW intrusion (Miles et al., 2016). In contrast, lower values of f_{sim} were observed in the ASP, DIS, and GIS, but f_{sim} gradually increased from the ASP toward the OA (range: −0.007–0.037), indicating sea ice melt due to increased solar heat during the summer in the MSIZ, spreading toward the OA (Fig. 3d).

The fluorescence intensity of C1 in the OA was 0.007 R.U. and gradually increased toward the DIS, varying between 0.008 and 0.013 R.U. (Fig. 3e). The mean fluorescence intensity of humic-like component in the global ocean surface layer (0–100 m) was about 0.007 R.U. (range: 0.004–0.011), and high fluorescence intensities (> 0.011 R.U.) were observed upwelling areas and areas receiving considerable amounts of terrestrial organic matter from surrounding continents (Jørgensen et al., 2011). Compared to the fluorescence intensity of the humic-like component in the global ocean surface layer, the high values of C1 (> 0.011 R.U.) were observed in front of the DIS, suggesting that the fluorescence intensity of C1 is associated with the CDW. Previous studies have reported that the fluorescence intensity of C1 gradually increased with depth (Chen and Bada, 1992; Determann et al., 1996; Stedmon and Markager, 2005a; Yamashita et al., 2007). Jørgensen et al. (2011) reported that the lowest fluorescence intensity of humic-like component (0.007 R.U.) was found in the surface layer and gradually increased by 0.012 R.U. at about 1000 m depth. Therefore, the high values of C1 fluorescence intensity in front of the ice shelves (> 0.011 R.U.) suggest that the humic-like C1 in the surface layer was derived from upwelling mCDW. However, the fluorescence intensity of C1 lower than the mean fluorescence intensity of the global ocean surface layer was observed in the surface layer in the OA and MSIZ, suggesting that the fluorescence intensity of C1 was photodegraded due to the exposure of the surface water to sunlight (Vecchio and Blough, 2002) and/or diluted by sea ice meltwater (Makarewicz et al., 2018).

3.3. Vertical distributions of freshwater fractions

Vertical transects of potential temperature (θ), salinity (S), and freshwater fractions (f_{mw} and f_{sim}) along a transect extending southeastward from the OA to the DIS (i.e., transect 1, Fig. 1) are shown in Fig. 4. As described in more detail by other studies (Yager et al., 2012, 2016; Randall-Goodwin et al., 2015; Sherrell et al., 2015; Miles et al., 2016), the distributions of S and θ show that the Amundsen Sea contained four major water masses: Antarctic Surface Water (AASW, defined as $S < 34.1$ and $-1.7\ ^{\circ}C < \theta < 0\ ^{\circ}C$), Winter Water (WW, defined as $S \approx 34.0$ and $\theta \approx -1.7\ ^{\circ}C$), mCDW (defined as $S > 34.5$ and $\theta \approx 0.5\ ^{\circ}C$), and CDW (defined as $S \approx 34.7$ and $\theta > 1.5\ ^{\circ}C$). In the OA, the layer between 300 and 800 m was occupied by pure CDW. The warm, salty tongue of CDW extended toward the DIS, becoming much colder and fresher by mixing with WW. At stations in the MSIZ (i.e., stations 50, 51, and 52) and ASP (i.e., stations 45, 48, and 49), mCDW was observed at depths below ~500 m from the shelf slope break to the coastal region along the Dotson Trough, leading to basal melting and thinning of the ice shelves (Rignot et al., 2013; Dutrieux et al., 2014; Randall-Goodwin et al., 2015). Above the mCDW layer, WW, reflecting convective mixing driven by brine rejection during sea ice formation during the winter, was observed extending from the AASW layer down to 400 m in depth. The AASW was variably warmer and fresher than the WW, because AASW is essentially WW modified to varying degrees by solar radiation and seasonal sea ice melt during the summer (Randall-Goodwin et al., 2015), and ranged in thickness from ~2 to 100 m.

The vertical section of f_{mw} exhibited vertical and regional variability along transect 1 (Fig. 4c). The f_{mw} varied from 0 to 0.028 along transect 1, with the highest values of f_{mw} (> 0.025) found in the layer between 300 m and the surface in front of the DIS, suggesting the upwelling of glacial meltwater at the DIS. In comparison, relatively lower f_{mw} values (0.017–0.024) were observed throughout the WW layer, indicating a redistribution of glacial meltwater and contributions from the CDW induced basal ice shelf meltwater (Randall-Goodwin et al., 2015). However, in the OA and the near bottom layer, the lowest f_{mw} values were observed, indicating CDW intrusion into the DIS and little mixing with the overlying WW along the trough. The f_{mw} values obtained in this study are in reasonable agreement with the ranges obtained by Randall-Goodwin et al. (2015), who reported that the highest meteoric water fractions were at the DIS outflow (2.1%) and large values in the WW layer (1.0–1.5%).

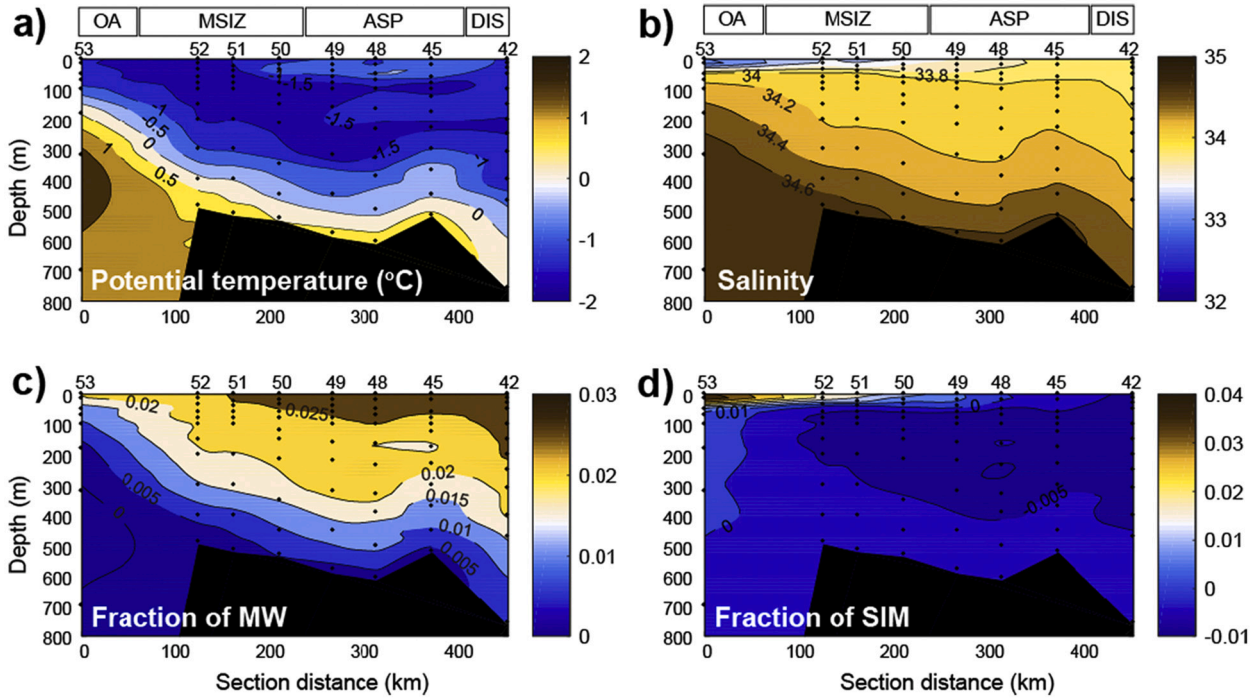

Fig. 4. Vertical distributions of (a) potential temperature (°C), (b) salinity, (c) meteoric water (f_{mw}), and (d) sea ice meltwater (f_{sim}) fractions obtained along transect 1 across the oceanic area (OA), marginal sea ice zone (MSIZ), Amundsen Sea polynya (ASP), and Dotson ice shelf (DIS). The station numbers are shown at the top of each figure. The upper panels in (a) and (b) show the sampling locations.

In the surface layer of the MSIZ and OA, positive f_{sim} values were observed, indicating net sea ice melt in these regions (Fig. 4d). However, the f_{sim} values were mostly negative throughout the water column in the ASP and DIS due to sea ice formation that injects brine into the underlying seawater. This indicates little contribution of sea ice meltwater to the freshwater budget below the surface layer in the Amundsen Sea during the austral summer.

In comparison, three water masses (i.e., AASW, WW, and mCDW) were identified in the western GIS (i.e., transect 2, Figs. 1 and 5). The vertical transects of θ, S, and freshwater fractions exhibited similar vertical distributions as those along transect 1, excluding OA (Fig. 5). The f_{mw} varied from 0 to 0.025 along transect 2, with higher values (0.019–0.025) in the upper 400 m (Fig. 5c). However, the f_{mw} values in the upper 400 m in the western GIS were somewhat lower than those in the DIS (0.021–0.028). Previous studies have reported that DIS basal meltwater is a major contributor to the freshwater budget of the ASP region (Randall-Goodwin et al., 2015; Miles et al., 2016; Jenkins et al., 2018). Furthermore, Nakayama et al. (2014) showed that modeled basal meltwater from the Amundsen Sea flows westward, with 36% reaching the Ross Sea, suggesting that some portion of f_{mw} in the western GIS could be derived from the Amundsen Sea. However, because of the difficulty in distinguishing how much of the glacial meltwater originated from the DIS or was generated locally in the western GIS, we cannot further determine the source strength for the meteoric water in the western GIS. Nevertheless, given that transect 1 is a known pathway of CDW intrusion (Ha et al., 2014), the relatively lower f_{mw} values in the western GIS are likely due to regional differences in the magnitude and duration of sub-glacial melting caused by CDW intrusion.

3.4. Vertical distributions and characteristics of the humic-like component

Vertical distributions of C1 fluorescence intensities along transects 1 and 2 are shown in Fig. 6a and b, respectively. Along transect 1, the fluorescence intensity of C1 varied from 0.007 to 0.021 R.U. (Fig. 6a), with higher values in the deeper layer and lower intensities in the surface water. In the OA, a C1 fluorescence intensity higher than 0.02 R.U. was identified in the layer occupied by pure CDW (Fig. 4a and b). Overall, higher values of C1 fluorescence intensity were observed along the pathway of CDW intrusions. The C1 fluorescence intensities along transect 2 exhibited similar vertical distributions to those observed along transect 1 excluding OA, varying from 0.011 to 0.019 (Fig. 6b).

The preponderance of studies of the humic-like component have reported a negative relationship with salinity, and thus humic-like component has a conservative behavior for mixing of water masses (Yamashita et al., 2008, 2011; Osburn and Stedmon, 2011; Ishii and Boyer, 2012; Tanaka et al., 2016; Zhu et al., 2018; Kim et al., 2019; Jung et al., 2021), suggesting that the humic-like component could be suitable as a tracer of water masses mixing (Gonçalves-Araujo et al., 2016). However, the production of the terrestrial humic-like component was observed during bacterial incubation experiments (Stedmon and Markager, 2005b; Shimotori et al., 2012), and the fluorescence intensity of the terrestrial humic-like component was correlated with AOU in the deep ocean (Yamashita et al., 2010), suggesting that the part of terrestrial humic-like component can be produced in situ. Here, we investigated the relationships between C1 fluorescence intensity and remineralization-related variables (i.e., apparent oxygen utilization (AOU), inorganic nutrients, and POC) (Fig. S2) to understand the characteristics of the humic-like component C1 in the Amundsen Sea. It is worth mentioning that, in the surface water, FDOM is mainly photodegraded by sunlight, whereas oxygen, nutrients, and POC are controlled by photosynthetic processes (Yamashita et al., 2007). Logvinova et al. (2015) reported significant losses (48–63%) in the fluorescence intensities of humic-like components by photodegradation in surface water samples collected in the ice-free western Arctic Ocean during 72 h solar exposure experiments, which were supported by both field and laboratory studies (Chen and Bada, 1992; Yamashita et al., 2007; Jørgensen et al., 2011). In our study region, the mean MLD and EZD were 27 ± 16 m and 35 ± 16 m in transect 1, and 23 ± 19 m and 20 ± 16 m in transect 2, respectively (Figs. 6a and b), suggesting that air-sea oxygen gas exchange and photodegradation of humic-like component C1 by sunlight are negligible in the water column below 50 m. Thus, we decided to use the dataset below 50 m to more clearly understand the relationships between the humic-like component C1 and remineralization-related variables. As shown in Fig. S2, the fluorescence

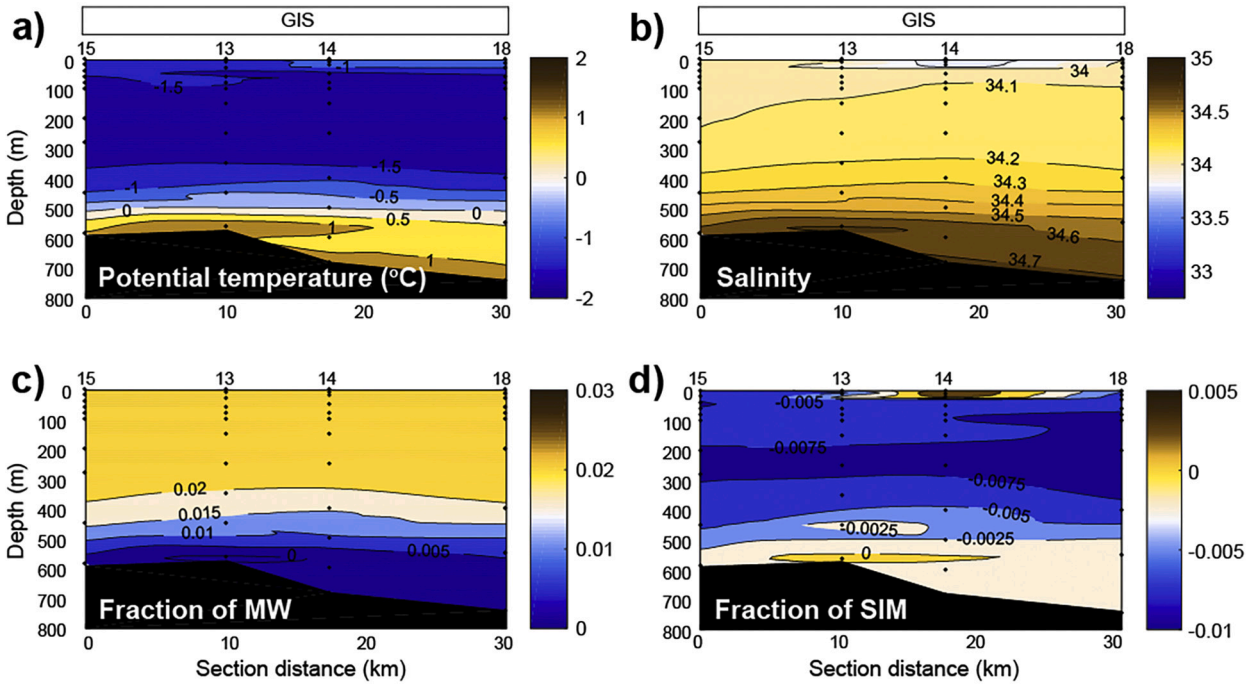

Fig. 5. Vertical distributions of (a) potential temperature (°C), (b) salinity, (c) meteoric water (f_{mw}), and (d) sea ice meltwater (f_{sim}) fractions obtained along transect 2 in front of the western Getz ice shelf (GIS). The station numbers are shown at the top of each figure. The upper panels in (a) and (b) show the sampling locations.

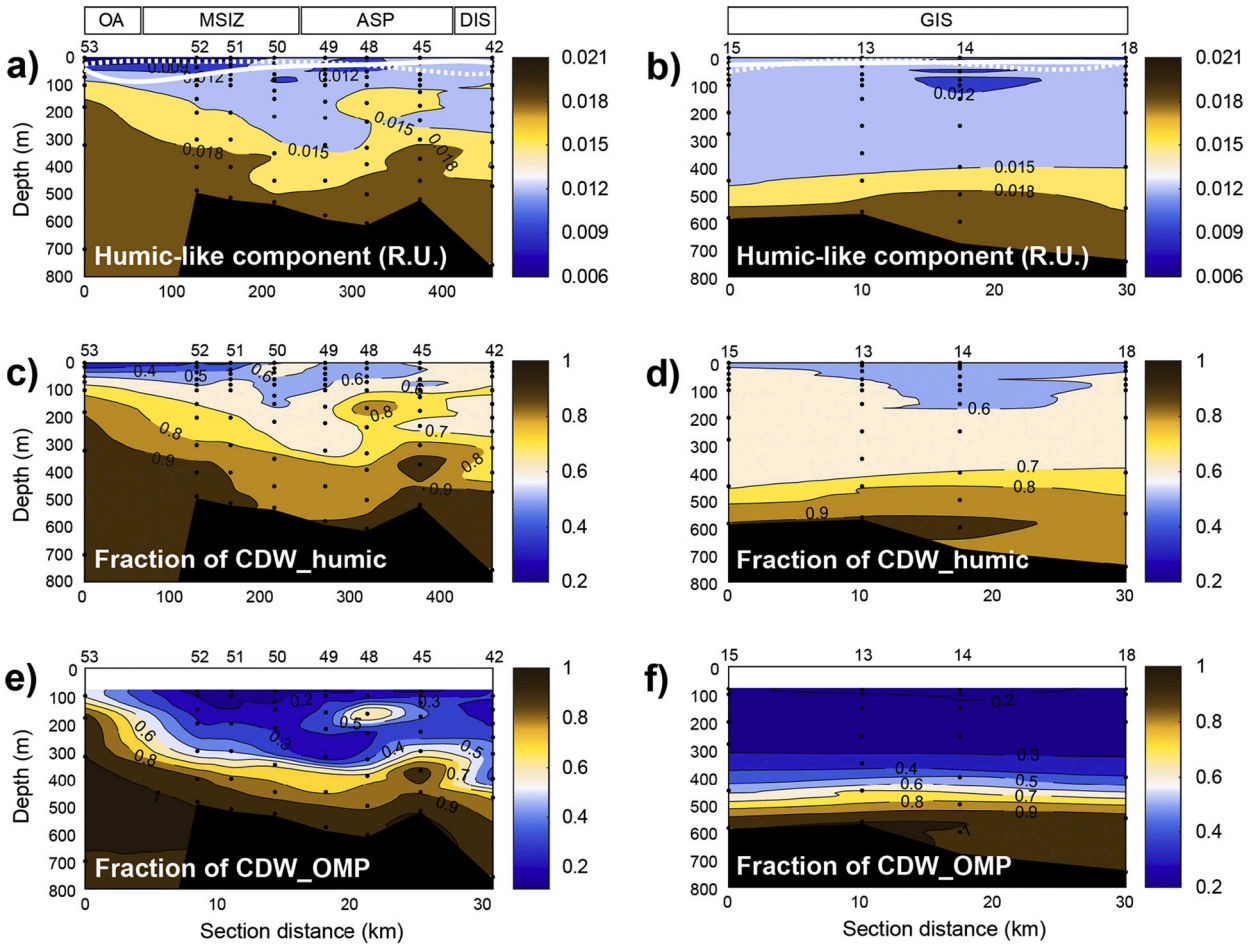

Fig. 6. Vertical distributions of (a and b) fluorescence intensity of the humic-like component (R.U.), (c and d) the Circumpolar Deep Water (CDW) fraction calculated using the humic-like component (f_{cdw_humic}), and (e and f) the CDW fraction calculated using optimum multiparameter (OMP) (f_{cdw_OMP}) along transects 1 and 2, respectively. The station numbers are shown at the top of each figure. The upper panels in (a) and (b) show the sampling locations. The white solid and dotted lines in (a) and (b) indicate the euphotic zone depth (EZD) and mixed layer depth (MLD), respectively.

intensity of C1 observed in transect 1 was positively correlated with AOU at depths greater than 50 m ($r = 0.93$, $p < 0.001$), $Si(OH)_4$ ($r = 0.87$, $p < 0.001$), $NO_2 + NO_3$ ($r = 0.54$, $p < 0.05$), and PO_4 ($r = 0.65$, $p < 0.001$), whereas it exhibited a negative relationship with POC ($r = -0.46$, $p < 0.05$). The fluorescence intensity of C1 observed in transect 2 also exhibited positive relationships with AOU below 50 m ($r = 0.95$, $p < 0.001$), $Si(OH)_4$ ($r = 0.88$, $p < 0.001$), $NO_2 + NO_3$ ($r = 0.56$, $p < 0.05$), and PO_4 ($r = 0.69$, $p < 0.001$), but was negatively correlated with POC ($r = -0.52$, $p < 0.05$). Among inorganic nutrients, $Si(OH)_4$ showed the most significant relationship with C1 fluorescence intensity. However, the main mechanism responsible for producing $Si(OH)_4$ in the water column (i.e., silica dissolution) is different from those for the other inorganic nutrients (i.e., remineralization) (Nelson et al., 1995; Cappellen et al., 2002). Silica dissolution is controlled by marine bacteria (Bidle and Azam, 1999) as well as other factors, including temperature, zooplankton grazing, and diatom aggregation (Nelson et al., 1995), suggesting that the marine bacterial activity can exert a critical role in silicon regeneration. Given that the humic-like component can be produced by microbial oxidation and degradation of organic matter, as mentioned above, the significant relationship between the humic-like component and $Si(OH)_4$ is likely due to bacteria-mediated silicon regeneration (Bidle and Azam, 1999). Arístegui et al. (2002) reported that ~90% of the oxygen consumption in the deep ocean is due to particle remineralization. Thus, the negative relationship between C1 and POC and its positive relationships with AOU and inorganic nutrients suggest that the humic-like component C1 can be partially derived from the remineralization of sinking particulate organic matter and bacterial respiration (Yamashita et al., 2007).

Although part of the humic-like component C1 can be derived from in situ, a positive linear relationship between the C1 fluorescence intensity and salinity was observed along transect 1 ($r = 0.89$, $p < 0.001$) and transect 2 ($r = 0.93$, $p < 0.001$) (Fig. S3), indicating the conservative behavior of C1 during the water masses mixing. In addition, the humic-like component has a long residence time (centuries to millennia) (Chen and Bada, 1992; Yamashita and Tanoue, 2008; Catalá et al., 2015), while the turnover time of meltwater-laden CDW waters in the western Amundsen Sea was estimated to be within decades (Kim et al., 2018). Furthermore, the humic-like C1 is resistant to internal processes of degradation (i.e., it is biologically unavailable, Ishii and Boyer, 2012), revealing conservative mixing behavior as aquatic systems transition from fresh to saline conditions. Thus, the humic-like component C1 can be used to trace the CDW, because the humic-like component C1 displays the conservative behavior on the time scale of physical mixing.

3.5. *Humic-like component as a tracer of CDW*

As mentioned above, pure CDW (defined as $S \approx 34.7$ and $\theta > 1.5$ °C) was observed in the layer between 300 and 800 m in the OA (Fig. 4a and b), where the C1 fluorescence intensity is 0.021 R.U. We therefore assume that 0.021 R.U. of C1 fluorescence intensity represents the C1 value for pure CDW. To assess the potential of the humic-like component C1 to act as a tracer of CDW in the Amundsen Sea, we used the following

equation to evaluate the fraction of CDW calculated using the humic-like component C1:

$$f_{cdw\_humic} = \frac{FI}{0.021} \quad (4)$$

where f_{cdw_humic} and *FI* refer to the fraction of CDW calculated using the humic-like component C1 and the observed C1 fluorescence intensity (R. U.), respectively. The f_{cdw_humic} values (i.e., calculated using Eq. (4)) along transects 1 and 2 are shown in Fig. 6c and d, respectively. The f_{cdw_humic} along transects 1 and 2 varied from 0.32 to 0.98 and 0.55 to 0.92, respectively, with higher values in the deeper layer and lower values in the shallower layer.

To evaluate the degree of overestimation or underestimation of f_{cdw_humic}, the fractions of CDW were calculated using OMP (f_{cdw_OMP}) along transects 1 and 2 and shown in Fig. 6e and f. In this study, we assumed that the calculation of CDW fraction using OMP provides a reliable estimate, which is used as a ground truth for the f_{cdw_humic}. The vertical distributions of f_{cdw_OMP} in transects 1 and 2 were similar to those of f_{cdw_humic}. The f_{cdw_OMP} varied from 0.12 to 1.00 along transect 1, with the highest values (> 0.998) in the OA at depths below 300 m. The higher f_{cdw_OMP} values (0.7–0.9) extended toward the DIS along the trough. In comparison, lower f_{cdw_OMP} values (0.2–0.4) were observed in the layer between 75 and 300 m except for OA, indicating mixing with the overlying WW and/or meteoric water, extending toward the DIS. The f_{cdw_OMP} varied from 0.17 to 1.00 along transect 2, with higher values (> 0.8) at depths below 500 m.

The humic-like component C1 exhibited significant positive relationships with f_{cdw_OMP} along transect 1 ($r = 0.94$, $p < 0.001$) and transect 2 ($r = 0.97$, $p < 0.001$) (Fig. 7a). However, the intercepts were − 1.14 for transect 1 and − 1.41 for transect 2 (Fig. 7a), indicating that about 0.011 R.U. of the humic-like component C1 fluorescence intensity remains when f_{cdw_OMP} value is zero. Biddle et al. (2017) reported that the use of specific end-member values could identify the "fresh" water masses, rather than "older" or cumulative water masses, because the values of θ, S, and DO vary by each season of observations. Thus, the offsets between humic-like component C1 fluorescence intensities and f_{cdw_OMP} values are likely due to the remained C1 that intruded into the Amundsen Sea during the other seasons. Nevertheless, the high correlations between C1 fluorescence intensities and f_{cdw_OMP} in transects 1 and 2 suggest the possibility that C1 can be used as a tracer for CDW.

In addition, statistically significant positive correlations were found between f_{cdw_humic} and f_{cdw_OMP} along transect 1 ($r = 0.94$, $p < 0.001$) and transect 2 ($r = 0.97$, $p < 0.001$) (Fig. 7b). However, the differences between f_{cdw_humic} and f_{cdw_OMP} were significant in the seawater samples collected in the upper 500 m, although similar f_{cdw_humic} and f_{cdw_OMP} values were observed in deep waters (> 500 m). The range of f_{cdw_humic} (0.5–1.0) was narrower than that of f_{cdw_OMP} (0.1–1.0), indicating that the f_{cdw_humic} values in the upper 500 m were overestimated due to the remained humic-like C1. To overcome this limitation, based on the assumption that f_{cdw_OMP} values are reliable, we used newly derived empirical equations (i.e., $f_{cdw\_OMP} = 105.17 \times C1 – 1.14$ for transect 1 and $f_{cdw\_OMP} = 126.04 \times C1 – 1.41$ for transect 2) (Fig. 7a) instead of Eq. (4) to estimate the fraction of CDW using the humic-like component. The fractions of CDW using these empirical equations ($f_{cdw\_humic\_empirical}$) were compared with the f_{cdw_OMP}, and the differences between two methods in transects 1 and 2 were 17 ± 12% and 17 ± 14%, respectively. Despite the differences between f_{cdw_OMP} and $f_{cdw\_humic\_empirical}$, significant positive relationships were observed between f_{cdw_OMP} and $f_{cdw\_humic\_empirical}$ along transect 1 ($r = 0.94$, $p < 0.001$) and transect 2 ($r = 0.97$, $p < 0.001$). In addition, the slopes and intercepts of regression line $f_{cdw\_humic\_empirical}$ on f_{cdw_OMP} are close to one and zero in transects 1 and 2, respectively, suggesting that humic-like component C1 could be used to trace the CDW and quantify the fraction of CDW. Our results therefore demonstrate that the humic-like component can be used as a reliable tracer of CDW below 75 m and above the bottom layer in the Amundsen

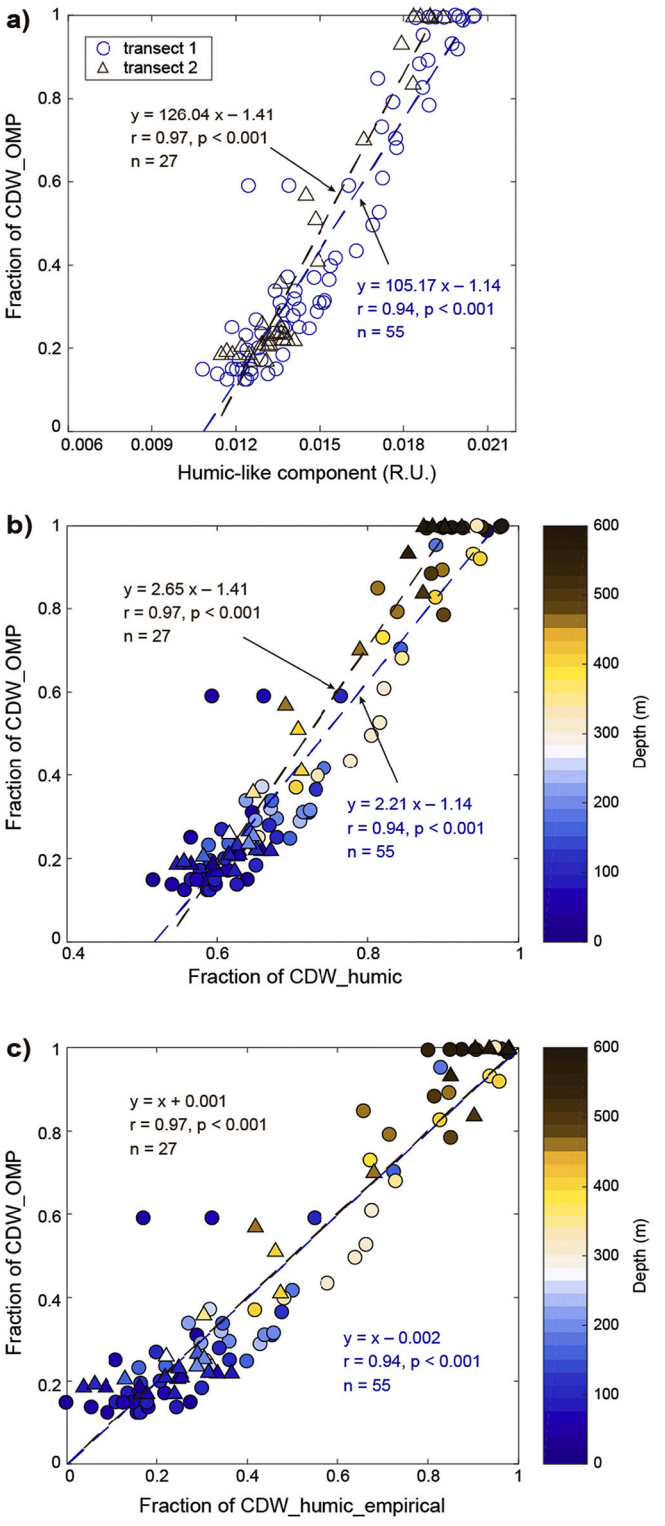

Fig. 7. Relationships of the Circumpolar Deep Water (CDW) fraction calculated using optimum multiparameter (f_{cdw_OMP}) with (a) humic-like component (R. U.) for transect 1 (blue circles) and transect 2 (brown triangles), (b) the CDW fraction calculated using the Eq. (4) (f_{cdw_humic}) as described in more detail in Section 3.5, and (c) the CDW fraction calculated using observation equations in Fig. 7(a) (y = 105.17 x – 1.14 for transect 1 and y = 126.04 x – 1.41 for transect 2) ($f_{cdw\_humic\_empirical}$). The colour bars in (b) and (c) show the sampling depth. The linear regression functions, correlation coefficients (r), *p*-values (p), and the numbers of samples (n) for transects 1 and 2 are also shown. (For interpretation of the references to colour in this figure legend, the reader is referred to the web version of this article.)

Sea.

3.6. Humic-like component as a tracer of glacial meltwater in the Amundsen Sea

As described in Section 3.5, we investigated the potential for the humic-like component to act as a tracer for CDW. In this section, we further investigate whether the humic-like component can be used as a tracer for glacial meltwater in the Amundsen Sea. The overall distributions of the humic-like component C1 and $\delta^{18}O$ can be understood in the context of water mass mixing, as illustrated by temperature-salinity diagrams. As shown in Fig. 8, the temperature-salinity diagram with colors indicating the humic-like component intensity is quite similar to that of $\delta^{18}O$. The highest values of C1 fluorescence intensity and $\delta^{18}O$ were observed in the CDW. These values gradually decreased along the CDW–WW mixing line. Between the CDW and WW end-members, the influence of subsurface glacial meltwater is observed (i.e., data points shift slightly from the CDW–WW mixing line toward the mixing line between CDW and meteoric water) (Randall-Goodwin et al., 2015). The values of C1 fluorescence intensity and $\delta^{18}O$ further decreased, bending from the CDW–WW mixing line toward the CDW–meteoric water mixing line due to the influence of meteoric water (i.e., dilution of C1 fluorescence intensity and lower $\delta^{18}O$ values in meteoric water). The similar distributions of the humic-like component and $\delta^{18}O$ make it possible to also use the humic-like component as a tracer of glacial meltwater in the Amundsen Sea.

As mentioned above, $\delta^{18}O$ is a useful tracer for meteoric water in the Amundsen Sea (Randall-Goodwin et al., 2015; Biddle et al., 2019). In general, meteoric water includes precipitation (snow and rain) and glacial meltwater. According to Bromwich et al. (2004), the mean annual precipitation for 1985–1999 in the Amundsen Sea was ~300 mm/year. In comparison, Rignot et al. (2013) reported that meltwater production in the DIS and GIS was 7.8 ± 0.6 and 4.3 ± 0.4 m/year, respectively, suggesting that the contribution of local precipitation to meteoric water is negligible in the Amundsen Sea. Therefore, we investigated the relationship between C1 fluorescence intensity and f_{mw} to examine the potential for the humic-like component to act as a tracer for glacial meltwater by assuming that f_{mw} in the Amundsen Sea represents the glacial meltwater fraction. Here we chose the dataset obtained below 50 m and above the bottom layer due to the limitations of the humic-like component related to photodegradation (see Section 3.4). We also excluded the dataset from the OA (i.e., station 53) where the influence of glacial meltwater was negligible (Fig. 4d). Statistically significant inverse relationships were observed between f_{mw} and C1 fluorescence intensity along transect 1 ($f_{mw} = -2.30 \times$ fluorescence intensity of the humic-like component +0.05, $r = -0.88$, $p < 0.001$) and transect 2 ($f_{mw} = -3.44 \times$ fluorescence intensity of the humic-like component +0.07, $r = -0.95$, $p < 0.001$) (Fig. 9a). Based on these relationships, we estimated the meteoric water fraction using the humic-like component (f_{mw_humic}) (Fig. 9b). Overall, the differences between f_{mw} and f_{mw_humic} in transects 1 and 2 were 28 ± 48% and 30 ± 94%, respectively, when f_{mw} was used as a ground truth. The large differences between f_{mw} and f_{mw_humic} were observed in the bottom layer where CDW or mCDW dominates. The f_{mw_humic} of the bottom layer tended to be overestimated, likely due to a mixture of mCDW and meltwater-laden mCDW. If the dataset from the bottom layers of transects 1 and 2 are excluded, the differences between f_{mw} and f_{mw_humic} decrease to 13 ± 11% and 12 ± 14%, respectively. Despite the differences between f_{mw} and f_{mw_humic}, significant positive relationships were observed between f_{mw} and f_{mw_humic} in transects 1 ($r = 0.88$, $p < 0.001$) and 2 ($r = 0.95$, $p < 0.001$). In addition, the slopes and intercepts of the relationships in transects 1 and 2 are close to one and zero, respectively, indicating that a reasonable method was applied with a high percentage of explained variance and that f_{mw} can be largely explained by f_{mw_humic}. Consequently, our results show that the humic-like component can be used as a tracer for glacial meltwater in the Amundsen Sea.

4. Conclusions

We herein demonstrated the potential for the humic-like component to trace CDW and glacial meltwater in the Amundsen Sea. During the cruise, the fluorescence intensity of the humic-like component varied from 0.007 to 0.021 R.U., with higher values in the deeper layer and lower intensities in the surface waters due to photodegradation by sunlight and dilution by sea ice meltwater. The highest fluorescence intensity of the humic-like component was observed in the deep layer of the OA that is occupied by pure CDW, reflecting the dominance of the humic-like component in CDW. In addition, the relationships between the fluorescence intensity of the humic-like component and remineralization-related variables suggest that the humic-like component is derived from the remineralization of sinking particulate organic matter and bacterial respiration.

The conservative behavior of the humic-like component was observed throughout the study region, with fluorescence intensities decreasing as salinity decreased. This characteristic allowed us to trace CDW. Our results for the comparison between f_{cdw_OMP} and

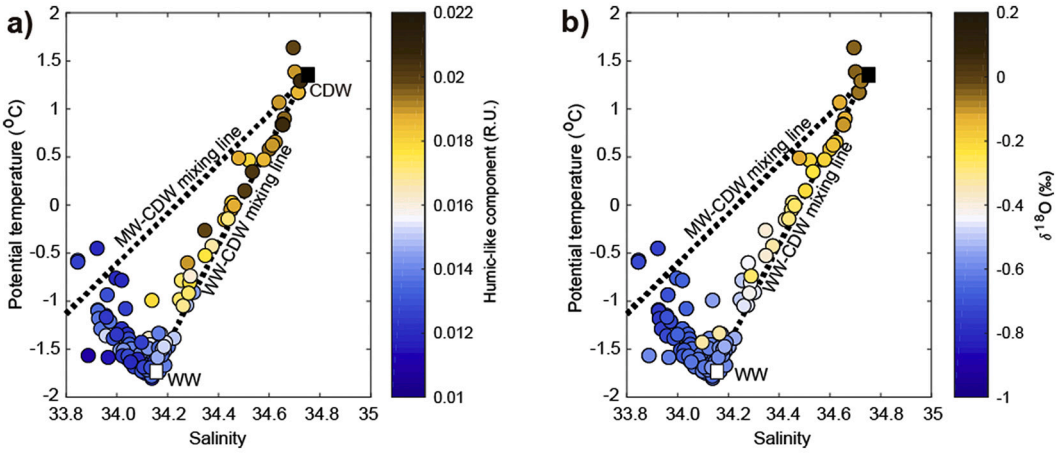

Fig. 8. Potential temperature-salinity (T-S) diagram of the Amundsen Sea. Colour bars in (a) and (b) show the fluorescence intensity of the humic-like component (R.U.) and the $\delta^{18}O$ values (‰), respectively. The black squares in (a) and (b) indicate the pure Circumpolar Deep Water (CDW) end-member observed at a depth of 700 m in the OA (station. 53). The white squares in (a) and (b) show the winter water (WW) end-member identified by Randall-Goodwin et al. (2015). The black short-dashed line indicates the mixing line between meteoric water and CDW (MW–CDW mixing line). The black long-dashed line indicates the mixing line between winter water and CDW (WW–CDW mixing line).

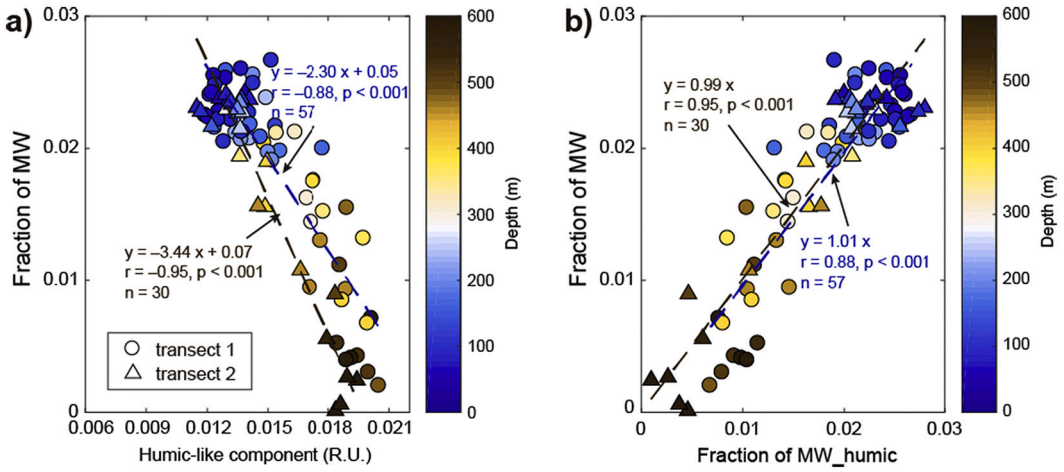

Fig. 9. Relationships between the meteoric water fraction calculated using $\delta^{18}O$ (f_{mw}) with (a) the humic-like component (R.U.) and (b) the meteoric water fraction calculated using the humic-like component (f_{mw_humic}) obtained along transect 1 (circles) and transect 2 (triangles). The dashed lines denote the linear regressions for transect 1 (blue dashed line) and transect 2 (brown dashed line), respectively. Note that samples collected in the upper 50 m were excluded from the scatter plots. The linear regression functions, correlation coefficients (r), p-values (p), and the numbers of samples (n) for transect 1 and 2 are also shown. (For interpretation of the references to colour in this figure legend, the reader is referred to the web version of this article.)

$f_{cdw\_humic\_empirical}$ show that the humic-like component C1 can be used to quantify the fraction of CDW as well as to trace the pathway of CDW. In addition, significant inverse relationships between f_{mw} and fluorescence intensity of the humic-like component suggest that the humic-like component can be used as a tracer of glacial meltwater as well, although there were regional differences in the inverse relationships due to regional differences in the magnitude and duration of sub-glacial melting caused by CDW intrusion.

Finally, the characteristics of the humic-like component in this study show that when other chemical tracers, such as $\delta^{18}O$ and noble gases, are not available, the humic-like component can be a useful tracer for identifying CDW and glacial meltwater in the Amundsen Sea. Although our dataset is not sufficiently complete to understand the distributions of CDW and glacial meltwater throughout the region, the results from this study are valuable for filling the data gap for the Amundsen Sea and can be useful for validating models of glacial meltwater and CDW distributions. In addition, our results provide additional insight into the hydrographic surveys focused on monitoring CDW circulation and glacial meltwater distribution in the Amundsen Sea. Because ice shelves and glaciers in the Amundsen Sea have been shrinking at a remarkable rate (Rignot et al., 2008), further studies are required to more clearly understand glacial meltwater and its impact on ocean circulation. Future studies should focus on the long-term monitoring of CDW and glacial meltwater in the Amundsen Sea.

CRediT author statement

MiHae Jeon: Investigation, Writing-Original draft preparation. *Jinyoung Jung:* Conceptualization, Supervision, Writing-Reviewing and Editing. *Mi Ok Park:* Supervision, Writing-Reviewing and Editing. *Shigeru Aoki:* Investigation, Writing-Reviewing and Editing. *Tae-Wan Kim:* Project administration, Funding acquisition, Writing-Reviewing and Editing. *Seung-Kyu Kim:* Resources.

Declaration of Competing Interest

The authors declare that they have no known competing financial interests or personal relationships that could have appeared to influence the work reported in this paper.

Acknowledgements

We are grateful to the captain and crew of the IBR/V *Araon* for their enthusiastic assistance during the ANA08B cruise. This study was supported by grants from the Korea Polar Research Institute (KOPRI) (PE21110). Shigeru Aoki was supported by Grand-in-Aid for Scientific Research (17H01615) of the MEXT of the Japanese Government.

Appendix A. Supplementary data

Supplementary data to this article can be found online at https://doi.org/10.1016/j.marchem.2021.104008.

References

Alderkamp, A.-C., Mills, M.M., van Dijken, G.L., Laan, P., Thuróczy, C.-E., Gerringa, L.J. A., de Baar, H.J.W., Payne, C.D., Visser, R.J.W., Buma, A.G.J., Arrigo, K.R., 2012. Iron from melting glaciers fuels phytoplankton blooms in the Amundsen Sea (Southern Ocean): phytoplankton characteristics and productivity. Deep Sea Res. Part II Top. Stud. Oceanogr. 71, 32–48. https://doi.org/10.1016/j.dsr2.2012.03.005.

Alderkamp, A.-C., van Dijken, G.L., Lowry, K.E., Connelly, T.L., Lagerström, M., Sherrell, R.M., Haskins, C., Rogalsky, E., Schofield, O., Stammerjohn, S.E., Yager, P. L., Arrigo, K.R., 2015. Fe availability drives phytoplankton photosynthesis rates during spring bloom in the Amundsen Sea Polynya, Antarctica. Elem. Sci. Anth. 3, 000043. https://doi.org/10.12952/journal.elementa.000043.

Arístegui, J., Duarte, C.M., Agustí, S., Doval, M., Álvarez-Salgado, X.A., Hansell, D.A., 2002. Dissolved organic carbon support of respiration in the Dark Ocean. Science 298, 1967. https://doi.org/10.1126/science.1076746.

Arrigo, K.R., van Dijken, G.L., 2003. Phytoplankton dynamics within 37 Antarctic coastal polynya systems. J. Geophys. Res.: Oceans 108. https://doi.org/10.1029/2002jc001739.

Biddle, L.C., Heywood, K.J., Kaiser, J., Jenkins, A., 2017. Glacial meltwater identification in the Amundsen Sea. J. Phys. Oceanogr. 47, 933–954. https://doi.org/10.1175/jpo-d-16-0221.1.

Biddle, L.C., Loose, B., Heywood, K.J., 2019. Upper Ocean Distribution of Glacial Meltwater in the Amundsen Sea, Antarctica. J. Geophys. Res.: Oceans 124, 6854–6870. https://doi.org/10.1029/2019jc015133.

Bidle, K.D., Azam, F., 1999. Accelerated dissolution of diatom silica by marine bacterial assemblages. Nature 397, 508–512. https://doi.org/10.1038/17351.

Bromwich, D.H., Guo, Z., Bai, L., Chen, Q., 2004. Modeled Antarctic precipitation. Part I: spatial and temporal variability. J. Clim. 17, 427–447. https://doi.org/10.1175/1520-0442(2004)017<0427:mappis>2.0.co;2.

Budillon, G., Pacciaroni, M., Cozzi, S., Rivaro, P., Catalano, G., Ianni, C., Cantoni, C., 2003. An optimum multiparameter mixing analysis of the shelf waters in the Ross Sea. Antarct. Sci. 15, 105–118. https://doi.org/10.1017/s095410200300110x.

Budillon, G., Bue, N.L., Siena, G., Spezie, G., 2010. Hydrographic characteristics of water masses and circulation in the Northern Ionian Sea. Deep Sea Res. Part II Top. Stud. Oceanogr. 57, 441–457. https://doi.org/10.1016/j.dsr2.2009.08.017.

Burdige, D.J., Kline, S.W., Chen, W., 2004. Fluorescent dissolved organic matter in marine sediment pore waters. Mar. Chem. 89, 289–311. https://doi.org/10.1016/j.marchem.2004.02.015.

Cappellen, P.V., Dixit, S., van Beusekom, J., 2002. Biogenic silica dissolution in the oceans: reconciling experimental and field-based dissolution rates. Global Biogeochem. Cycles 16. https://doi.org/10.1029/2001gb001431, 23-1-23–10.

Carlson, C.A., Hansell, D.A., Peltzer, E.T., Smith, W.O., 2000. Stocks and dynamics of dissolved and particulate organic matter in the southern Ross Sea, Antarctica. Deep Sea Res. Part II Top. Stud. Oceanogr. 47, 3201–3225.

Carpenter, James H., 1965. The Chesapeake Bay institute technique for the Winkler dissolved oxygen method. Limnol. Oceanogr. 10, 141–143. https://doi.org/10.4319/lo.1965.10.1.0141.

Castillo, C.E.D., Coble, P.G., 2000. Seasonal variability of the colored dissolved organic matter during the 1994–95 NE and SW monsoons in the Arabian Sea. Deep Sea Res. Part II Top. Stud. Oceanogr. 47, 1563–1579. https://doi.org/10.1016/s0967-0645(99)00154-x.

Catalá, T.S., Reche, I., Fuentes-Lema, A., Romera-Castillo, C., Nieto-Cid, M., Ortega-Retuerta, E., Calvo, E., Álvarez, M., Marrasé, C., Stedmon, C.A., Álvarez-Salgado, X. A., 2015. Turnover time of fluorescent dissolved organic matter in the dark global ocean. Nat. Commun. 6, 5986. https://doi.org/10.1038/ncomms6986.

Chari, N.V.H.K., Keerthi, S., Sarma, N.S., Pandi, S.R., Chiranjeevulu, G., Kiran, R., Koduru, U., 2013. Fluorescence and absorption characteristics of dissolved organic matter excreted by phytoplankton species of western bay of Bengal under axenic laboratory condition. J. Exp. Mar. Biol. Ecol. 445, 148–155. https://doi.org/10.1016/j.jembe.2013.03.015.

Chen, R.F., Bada, J.L., 1992. The fluorescence of dissolved organic matter in seawater. Mar. Chem. 37, 191–221. https://doi.org/10.1016/0304-4203(92)90078-o.

Chen, M., Jung, J., Lee, Y.K., Hur, J., 2018. Surface accumulation of low molecular weight dissolved organic matter in surface waters and horizontal off-shelf spreading of nutrients and humic-like fluorescence in the Chukchi Sea of the Arctic Ocean. Sci. Total Environ. 639, 624–632. https://doi.org/10.1016/j.scitotenv.2018.05.205.

Chen, M., Jung, J., Lee, Y.K., Kim, T.-W., Hur, J., 2019. Production of tyrosine-like fluorescence and labile chromophoric dissolved organic matter (DOM) and low surface accumulation of low molecular weight-dominated DOM in a productive Antarctic Sea. Mar. Chem. 213, 40–48. https://doi.org/10.1016/j.marchem.2019.04.009.

Cisewski, B., Strass, V.H., Losch, M., Prandke, H., 2008. Mixed layer analysis of a mesoscale eddy in the Antarctic Polar Front Zone. J. Geophys. Res.: Oceans 113. https://doi.org/10.1029/2007jc004372.

Coble, P.G., 1996. Characterization of marine and terrestrial DOM in seawater using excitation-emission matrix spectroscopy. Mar. Chem. 51, 325–346. https://doi.org/10.1016/0304-4203(95)00062-3.

Coble, P.G., 2007. Marine optical biogeochemistry: the chemistry of ocean color. Chem. Rev. 38 https://doi.org/10.1002/chin.200720265.

Coble, P., Nelson, N., 2009. Optical analysis of chromophoric dissolved organic matter. In: Practical Guidelines for the Analysis of Seawater. https://doi.org/10.1201/9781420073072.ch5.

Determann, S., Reuter, R., Willkomm, R., 1996. Fluorescent matter in the eastern Atlantic Ocean. Part 2: vertical profiles and relation to water masses. Deep Sea res. Part I Oceanogr. Res. Pap. 43, 345–360. https://doi.org/10.1016/0967-0637(96)00008-8.

Dubnick, A., Barker, J., Sharp, M., Wadham, J., Lis, G., Telling, J., Fitzsimons, S., Jackson, M., 2010. Characterization of dissolved organic matter (DOM) from glacial environments using total fluorescence spectroscopy and parallel factor analysis. Ann. Glaciol. 51, 111–122. https://doi.org/10.3189/172756411795931912.

Dutrieux, P., Rydt, J.D., Jenkins, A., Holland, P.R., Ha, H.K., Lee, S.H., Steig, E.J., Ding, Q., Abrahamsen, E.P., Schröder, M., 2014. Strong sensitivity of Pine Island ice-shelf melting to climatic variability. Science 343, 174–178. https://doi.org/10.1126/science.1244341.

Fang, L., Lee, S., Lee, S.-A., Hahm, D., Kim, G., Druffel, E.R.M., Hwang, J., 2020. Removal of refractory dissolved organic carbon in the Amundsen Sea, Antarctica. Sci. Rep. 10, 1213. https://doi.org/10.1038/s41598-020-57870-6.

Fellman, J.B., D'Amore, D.V., Hood, E., 2008. An evaluation of freezing as a preservation technique for analyzing dissolved organic C, N and P in surface water samples. Sci. Total Environ. 392, 305–312. https://doi.org/10.1016/j.scitotenv.2007.11.027.

Frants, M., Gille, S.T., Hewes, C.D., Holm-Hansen, O., Kahru, M., Lombrozo, A., Measures, C.I., Mitchell, B.G., Wang, H., Zhou, M., 2013. Optimal multiparameter analysis of source water distributions in the Southern Drake Passage. Deep Sea Res. Part II Top. Stud. Oceanogr. 90, 31–42. https://doi.org/10.1016/j.dsr2.2012.06.002.

Gerringa, L.J.A., Alderkamp, A.-C., Laan, P., Thuróczy, C.-E., Baar, H.J.W.D., Mills, M.M., van Dijken, G.L., van Haren, H., Arrigo, K.R., 2012. Iron from melting glaciers fuels the phytoplankton blooms in Amundsen Sea (Southern Ocean): Iron biogeochemistry. Deep Sea Res. Part II Top. Stud. Oceanogr. 71, 16–31. https://doi.org/10.1016/j.dsr2.2012.03.007.

Gonçalves-Araujo, R., Granskog, M.A., Bracher, A., Azetsu-Scott, K., Dodd, P.A., Stedmon, C.A., 2016. Using fluorescent dissolved organic matter to trace and distinguish the origin of Arctic surface waters. Sci. Rep. 6, 33978. https://doi.org/10.1038/srep33978.

Gordon, L.I., Jr Jennings, C.J., Ross, A.A., Krest, J.M., 1993. A Suggested Protocol for Continuous Flow Automated Analysis of Seawater Nutrients (phosphate, nitrate, nitrite and silicic acid) in the WOCE Hydrographic Program and the Joint Global Ocean Fluxes Study. WOCE Hydrographic Program Office, Methods Manual WHPO, Corvallis.

Ha, H.K., Wåhlin, A.K., Kim, T.W., Lee, S.H., Lee, J.H., Lee, H.J., Hong, C.S., Arneborg, L., Björk, G., Kalén, O., 2014. Circulation and modification of warm deep water on the Central Amundsen shelf. J. Phys. Oceanogr. 44, 1493–1501. https://doi.org/10.1175/jpo-d-13-0240.1.

Ishii, S.K.L., Boyer, T.H., 2012. Behavior of reoccurring PARAFAC components in fluorescent dissolved organic matter in natural and engineered systems: a critical review. Environ. Sci. Technol. 46, 2006–2017. https://doi.org/10.1021/es2043504.

Jacobs, S.S., Jenkins, A., Giulivi, C.F., Dutrieux, P., 2011. Stronger ocean circulation and increased melting under Pine Island glacier ice shelf. Nat. Geosci. 4, 519–523. https://doi.org/10.1038/ngeo1188.

Jacobs, S., Jenkins, A., Hellmer, H., Giulivi, C., Nitsche, F., Huber, B., Guerrero, R., 2012. The Amundsen Sea and the Antarctic ice sheet. Oceanography 25, 154–163. https://doi.org/10.5670/oceanog.2012.90.

Jenkins, A., Dutrieux, P., Jacobs, S.S., McPhail, S.D., Perrett, J.R., Webb, A.T., White, D., 2010. Observations beneath Pine Island glacier in West Antarctica and implications for its retreat. Nat. Geosci. 3, 468–472.

Jenkins, A., Shoosmith, D., Dutrieux, P., Jacobs, S., Kim, T.W., Lee, S.H., Ha, H.K., Stammerjohn, S., 2018. West Antarctic ice sheet retreat in the Amundsen Sea driven by decadal oceanic variability. Nat. Geosci. 11, 733–738.

Jiang, T., Chen, X., Wang, D., Liang, J., Bai, W., Zhang, C., Wang, Q., Wei, S., 2018. Dynamics of dissolved organic matter (DOM) in a typical inland lake of the three gorges reservoir area: fluorescent properties and their implications for dissolved mercury species. J. Environ. Manag. 206, 418–429. https://doi.org/10.1016/j.jenvman.2017.10.048.

Jørgensen, L., Stedmon, C.A., Kragh, T., Markager, S., Middelboe, M., Søndergaard, M., 2011. Global trends in the fluorescence characteristics and distribution of marine dissolved organic matter. Mar. Chem. 126, 139–148. https://doi.org/10.1016/j.marchem.2011.05.002.

Jourdain, N.C., Mathiot, P., Merino, N., Durand, G., Sommer, J.L., Spence, P., Dutrieux, P., Madec, G., 2017. Ocean circulation and sea-ice thinning induced by melting ice shelves in the A mundsen Sea. J. Geophys. Res.: Oceans 122, 2550–2573.

Jung, J., Hong, S.-B., Chen, M., Hur, J., Jiao, L., Lee, Y., Park, K., Hahm, D., Choi, J.-O., Yang, E.J., 2020. Characteristics of methanesulfonic acid, non-sea-salt sulfate and organic carbon aerosols over the Amundsen Sea, Antarctica. Atmos. Chem. Phys. 20, 5405–5424.

Jung, J., Son, J.E., Lee, Y.K., Cho, K.-H., Lee, Y., Yang, E.J., Kang, S.-H., Hur, J., 2021. Tracing riverine dissolved organic carbon and its transport to the halocline layer in the Chukchi Sea (western Arctic Ocean) using humic-like fluorescence fingerprinting. Sci. Total Environ. 772, 145542. https://doi.org/10.1016/j.scitotenv.2021.145542.

Kida, M., Kojima, T., Tanabe, Y., Hayashi, K., Kudoh, S., Maie, N., Fujitake, N., 2019. Origin, distributions, and environmental significance of ubiquitous humic-like fluorophores in Antarctic lakes and streams. Water Res. 163, 114901. https://doi.org/10.1016/j.watres.2019.114901.

Kim, I., Hahm, D., Rhee, T.S., Kim, T.W., Kim, C., Lee, S., 2016. The distribution of glacial meltwater in the Amundsen Sea, Antarctica, revealed by dissolved helium and neon. J. Geophys. Res.: Oceans 121, 1654–1666. https://doi.org/10.1002/2015jc011211.

Kim, B., Lee, S., Kim, M., Hahm, D., Rhee, T.S., Hwang, J., 2018. An investigation of gas exchange and water circulation in the Amundsen Sea based on dissolved inorganic radiocarbon. Geophys. Res. Lett. 45, 12,368–12,375. https://doi.org/10.1029/2018gl079464.

Kim, J., Kim, Y., Kang, H.-W., Kim, S.H., Rho, T., Kang, D.-J., 2019. Tracing water mass fractions in the deep western Indian Ocean using fluorescent dissolved organic matter. Mar. Chem. 218, 103720. https://doi.org/10.1016/j.marchem.2019.103720.

Kirk, J.T., 1994. Light and Photosynthesis in Aquatic Ecosystems. Cambridge university press.

Logvinova, C.L., Frey, K.E., Mann, P.J., Stubbins, A., Spencer, R.G.M., 2015. Assessing the potential impacts of declining Arctic sea ice cover on the photochemical degradation of dissolved organic matter in the Chukchi and Beaufort Seas. J. Geophys. Res. 120, 2326–2344. https://doi.org/10.1002/2015jg003052.

Makarewicz, A., Kowalczuk, P., Sagan, S., Granskog, M.A., Pavlov, A.K., Zdun, A., Borzycka, K., Zabłocka, M., 2018. Characteristics of chromophoric and fluorescent dissolved organic matter in the Nordic seas. Ocean Sci. 14, 543–562.

Mendoza, W.G., Weiss, E.L., Schieber, B., Mitchell, B.G., 2017. Controls on the distribution of fluorescent dissolved organic matter during an under-ice algal bloom in the western Arctic Ocean. Glob. Biogeochem. Cycles 31, 1118–1140. https://doi.org/10.1002/2016gb005569.

Meredith, M.P., Brandon, M.A., Wallace, M.I., Clarke, A., Leng, M.J., Renfrew, I.A., Lipzig, N.P.V., King, J.C., 2008. Variability in the freshwater balance of northern Marguerite Bay, Antarctic peninsula: results from δ18O. Deep Sea Res. Part II Top. Stud. Oceanogr. 55, 309–322.

Miles, T., Lee, S.H., Wåhlin, A., Ha, H.K., Kim, T.W., Assmann, K.M., Schofield, O., 2016. Glider observations of the Dotson Ice Shelf outflow. Deep Sea Res. Part II Top. Stud. Oceanogr. 123, 16–29.

Mopper, K., Feng, Z., Bentjen, S.B., Chen, R.F., 1996. Effects of cross-flow filtration on the absorption and fluorescence properties of seawater. Mar. Chem. 55, 53–74.

Murphy, K.R., Stedmon, C.A., Wenig, P., Bro, R., 2013. OpenFluor– an online spectral library of auto-fluorescence by organic compounds in the environment. Anal Methods-uk 6, 658–661. https://doi.org/10.1039/c3ay41935e.

Nakamura, K., Aoki, S., Yoshimura, K., Kurita, N., 2014. Distribution of oxygen isotope ratio of precipitation in the Atlantic-Indian sectors of the Southern Ocean. Sola. 10, 154–157.

Nakayama, Y., Timmermann, R., Rodehacke, C.B., Schröder, M., Hellmer, H.H., 2014. Modeling the spreading of glacial meltwater from the Amundsen and Bellingshausen seas. Geophys. Res. Lett. 41, 7942–7949.

Nelson, D.M., Trrguer, P., Brzezinski, M.A., Leynaert, A., Qurguiner, B., 1995. Production and dissolution of biogenic silica in the ocean: revised global estimates, comparison with regional data and relationship to biogenic sedimentation. Glob. Biogeochem. Cycles 9, 359–372.

Osburn, C.L., Stedmon, C.A., 2011. Linking the chemical and optical properties of dissolved organic matter in the Baltic–North Sea transition zone to differentiate three allochthonous inputs. Mar. Chem. 126, 281–294.

Östlund, H.G., Hut, G., 1984. Arctic Ocean water mass balance from isotope data. J. Geophys. Res.: Oceans 89, 6373–6381.

Pardo, P.C., Pérez, F.F., Velo, A., Gilcoto, M., 2012. Water masses distribution in the Southern Ocean: improvement of an extended OMP (eOMP) analysis. Prog. Oceanogr. 103, 92–105. https://doi.org/10.1016/j.pocean.2012.06.002.

Park, J., Kuzminov, F.I., Bailleul, B., Yang, E.J., Lee, S., Falkowski, P.G., Gorbunov, M.Y., 2017. Light availability rather than Fe controls the magnitude of massive phytoplankton bloom in the Amundsen Sea polynyas, Antarctica. Limnol. Oceanogr. 62, 2260–2276. https://doi.org/10.1002/lno.10565.

Poole, R., Tomczak, M., 1999. Optimum multiparameter analysis of the water mass structure in the Atlantic Ocean thermocline. Deep Sea Res. Part I Oceanogr. Res. Pap. 46, 1895–1921. https://doi.org/10.1016/s0967-0637(99)00025-4.

Pritchard, Hd, Ligtenberg, S.R., Fricker, H.A., Vaughan, D.G., van den Broeke, M.R., Padman, L., 2012. Antarctic ice-sheet loss driven by basal melting of ice shelves. Nature 484, 502–505.

Randall-Goodwin, E., Meredith, M.P., Jenkins, A., Yager, P.L., Sherrell, R.M., Abrahamsen, E.P., Guerrero, R., Yuan, X., Mortlock, R.A., Gavahan, K., Alderkamp, A.-C., Ducklow, H., Robertson, R., Stammerjohn, S.E., 2015. Freshwater distributions and water mass structure in the Amundsen Sea Polynya region, Antarctica. Elem. Sci. Anth. 3, 000065. https://doi.org/10.12952/journal.elementa.000065.

Rignot, E., Bamber, J.L., Broeke, M.R.V.D., Davis, C., Li, Y., Berg, W.J.V.D., Meijgaard, E. V., 2008. Recent Antarctic ice mass loss from radar interferometry and regional climate modelling. Nat. Geosci. 1, 106–110.

Rignot, E., Jacobs, S., Mouginot, J., Scheuchl, B., 2013. Ice-shelf melting around Antarctica. Science 341, 266–270.

Rochelle-Newall, E., Hulot, F.D., Janeau, J.L., Merroune, A., 2014. CDOM fluorescence as a proxy of DOC concentration in natural waters: a comparison of four contrasting tropical systems. Environ. Monit. Assess. 186, 589–596. https://doi.org/10.1007/s10661-013-3401-2.

Shen, Y., Benner, R., 2018. Mixing it up in the ocean carbon cycle and the removal of refractory dissolved organic carbon. Sci. Rep. 8, 2542. https://doi.org/10.1038/s41598-018-20857-5.

Shepherd, A., Ivins, E., Rignot, E., Smith, B., Broeke, M.V.D., Velicogna, I., Whitehouse, P., Briggs, K., Joughin, I., Krinner, G., 2018. Mass balance of the Antarctic ice sheet from 1992 to 2017. Nature 558, 219–222.

Sherrell, R., Lagerström, M., Forsch, K., Stammerjohn, S., Yager, P., Miller, L.A., 2015. Dynamics of dissolved iron and other bioactive trace metals (Mn, Ni, Cu, Zn) in the Amundsen Sea Polynya, AntarcticaBioactive trace metal dynamics in the Amundsen Sea Polynya, Antarctica. Elem. Sci. Anth. 3.

Shimotori, K., Watanabe, K., Hama, T., 2012. Fluorescence characteristics of humic-like fluorescent dissolved organic matter produced by various taxa of marine bacteria. Aquat. Microb. Ecol. 65, 249–260. https://doi.org/10.3354/ame01552.

Silvano, A., Rintoul, S.R., Peña-Molino, B., Hobbs, W.R., van Wijk, E., Aoki, S., Tamura, T., Williams, G.D., 2018. Freshening by glacial meltwater enhances melting of ice shelves and reduces formation of Antarctic Bottom Water. Sci. Adv. 4, eaap9467.

Spencer, R.G.M., Bolton, L., Baker, A., 2007. Freeze/thaw and pH effects on freshwater dissolved organic matter fluorescence and absorbance properties from a number of UK locations. Water Res. 41, 2941–2950. https://doi.org/10.1016/j.watres.2007.04.012.

Stedmon, C.A., Bro, R., 2008. Characterizing dissolved organic matter fluorescence with parallel factor analysis: a tutorial. Limnol. Oceanogr. Methods 6, 572–579.

Stedmon, C.A., Markager, S., 2005a. Resolving the variability in dissolved organic matter fluorescence in a temperate estuary and its catchment using PARAFAC analysis. Limnol. Oceanogr. 50, 686–697.

Stedmon, C.A., Markager, S., 2005b. Tracing the production and degradation of autochthonous fractions of dissolved organic matter by fluorescence analysis. Limnol. Oceanogr. 50, 1415–1426. https://doi.org/10.4319/lo.2005.50.5.1415.

Stedmon, C.A., Nelson, N.B., 2015. The optical properties of DOM in the ocean. In: Undefined, Biogeochemistry of Marine Dissolved Organic Matter. Elsevier, pp. 481–508.

Stedmon, C.A., Markager, S., Bro, R., 2003. Tracing dissolved organic matter in aquatic environments using a new approach to fluorescence spectroscopy. Mar. Chem. 82, 239–254.

Stedmon, C.A., Thomas, D.N., Papadimitriou, S., Granskog, M.A., Dieckmann, G.S., 2011. Using fluorescence to characterize dissolved organic matter in Antarctic sea ice brines. J. Geophys. Res. 116. https://doi.org/10.1029/2011jg001716.

Tanaka, K., Takesue, N., Nishioka, J., Kondo, Y., Ooki, A., Kuma, K., Hirawake, T., Yamashita, Y., 2016. The conservative behavior of dissolved organic carbon in surface waters of the southern Chukchi Sea, Arctic Ocean, during early summer. Sci. Rep. 6, 1–10.

Thurman, E., 1985. Aquatic humic substances. In: Undefined, Organic Geochemistry of Natural Waters. Springer, pp. 273–361.

Tomczak, M., Large, D.G.B., 1989. Optimum multiparameter analysis of mixing in the thermocline of the eastern Indian Ocean. J. Geophys. Res. Oceans 94, 16141–16149. https://doi.org/10.1029/jc094ic11p16141.

Vecchio, R.D., Blough, N.V., 2002. Photobleaching of chromophoric dissolved organic matter in natural waters: kinetics and modeling. Mar. Chem. 78, 231–253.

Yager, P.L., Sherrell, R.M., Stammerjohn, S.E., Alderkamp, A.-C., Schofield, O., Abrahamsen, E.P., Arrigo, K.R., Bertilsson, S., Garay, D.L., Guerrero, R., 2012. ASPIRE: the Amundsen Sea polynya international research expedition. Oceanography 25, 40–53.

Yager, P., Sherrell, R., Stammerjohn, S., Ducklow, H., Schofield, O., Ingall, E., Wilson, S., Lowry, K., Williams, C., Riemann, L., Bertilsson, S., Alderkamp, A.-C., Dinasquet, J., Logares, R., Richert, I., Sipler, R., Melara, A., Mu, L., Newstead, R., Post, A., Swalethorp, R., van Dijken, G., 2016. A carbon budget for the Amundsen Sea Polynya, Antarctica: estimating net community production and export in a highly productive polar ecosystem. Elementa. 4, 000140. https://doi.org/10.12952/journal.elementa.000140.

Yamashita, Y., Tanoue, E., 2008. Production of bio-refractory fluorescent dissolved organic matter in the ocean interior. Nat. Geosci. 1, 579–582. https://doi.org/10.1038/ngeo279.

Yamashita, Y., Tsukasaki, A., Nishida, T., Tanoue, E., 2007. Vertical and horizontal distribution of fluorescent dissolved organic matter in the Southern Ocean. Mar. Chem. 106, 498–509. https://doi.org/10.1016/j.marchem.2007.05.004.

Yamashita, Y., Jaffe, R., Maie, N., Tanoue, E., 2008. Assessing the dynamics of dissolved organic matter (DOM) in coastal environments by excitation emission matrix fluorescence and parallel factor analysis (EEM-PARAFAC). Limnol. Oceanogr. 53, 1900–1908.

Yamashita, Y., Cory, R.M., Nishioka, J., Kuma, K., Tanoue, E., Jaffé, R., 2010. Fluorescence characteristics of dissolved organic matter in the deep waters of the Okhotsk Sea and the northwestern North Pacific Ocean. Deep Sea Res. Part II Top. Stud. Oceanogr. 57, 1478–1485. https://doi.org/10.1016/j.dsr2.2010.02.016.

Yamashita, Y., Panton, A., Mahaffey, C., Jaffé, R., 2011. Assessing the spatial and temporal variability of dissolved organic matter in Liverpool Bay using excitation–emission matrix fluorescence and parallel factor analysis. Ocean Dyn. 61, 569–579. https://doi.org/10.1007/s10236-010-0365-4.

Zhu, W.-Z., Zhang, J., Yang, G.-P., 2018. Mixing behavior and photobleaching of chromophoric dissolved organic matter in the Changjiang River estuary and the adjacent East China Sea. Estuar. Coast. Shelf Sci. 207, 422–434.